A COMPUTATIONAL FRAMEWORK TO UNDERSTAND VASCULAR ADAPTATION

A Dissertation

Presented to

the Faculty of the Department of Computer Science

University of Houston

In Partial Fulfillment

of the Requirements for the Degree

Doctor of Philosophy

By

Mahbubur Rahman

May 2015

A COMPUTATIONAL FRAMEWORK TO UNDERSTAND VASCULAR ADAPTATION

Mahbubur Rahman

APPROVED:

Dr. Marc Garbey, Chairman
Dept. of Computer Science

Dr. Scott A. Berceli, Co-Chairman
Dept. of Surgery, University of Florida

Dr. Nikolaos V. Tsekos
Dept. of Computer Science

Dr. Edgar Gabriel
Dept. of Computer Science

Dr. Victoria Hillford
Dept. of Computer Science

Dean, College of Natural Sciences and Mathematics

Acknowledgements

My special thanks and sincere appreciation go to Dr. Marc Garbey, who as a chairperson of my PhD committee has helped and guided me through my research from the very beginning to the end. I would also like to thank co-chairman of my PhD committee, Dr. Scott A. Berceli for his generous support, guidance and encouragement. My sincere appreciation goes to my other committee members Dr. Nicolaos Tsekos, Dr. Edgar Gabriel and Dr. Victoria Hillford. Special thanks go to the National Institute of Health (NIH) for supporting this project and the high performance computing center at the University of Houston, where the simulation program has been run. Additionally, I would like to thank all of my lab mates at the modeling and computational science (MCS) lab of the University of Houston. Last, but not the least; my deepest gratitude goes to my parents and family members for their continuous encouragement, patience and support without which I cannot achieve this goal.

A COMPUTATIONAL FRAMEWORK TO UNDERSTAND VASCULAR ADAPTATION

An Abstract of a Dissertation

Presented to

the Faculty of the Department of Computer Science

University of Houston

In Partial Fulfillment

of the Requirements for the Degree

Doctor of Philosophy

By

Mahbubur Rahman

May 2015

Abstract

Researchers have been continuously applying a wide variety of approaches to understand vascular adaptation over the past two decades. However, the specific cause/effect or links between the hemodynamic factors, inflammatory biochemical mediators, cellular effectors and vascular occlusive phenotype remain unexplained still today. To explain these biological phenomena, we have introduced a multi-scale computational framework to systematically test many hypotheses associated with the vascular adaptation and finally applied this framework to explain some widely observed clinical and experimental cases. Our framework incorporates the cellular activities inside the vein graft influenced by the shear stress and tension, which are two of the most important environmental factors in the vascular adaptation. This is a hybrid agent based model (ABM) coupled with the partial differential equations (PDEs) associated with the calculation of the shear stress. Based on the computational framework, we have designed and developed a modular, adaptive, efficient and scalable simulation program so that we can explain some specific pattern formations associated with the vascular adaptation by pattern recognition algorithms of the framework in real time. Finally, we have coupled a genetic algorithm with the framework to verify the fact that a combination of interesting patterns associated with the vascular adaptation can be regenerated in a multivariate data analysis environment. As a result, this research will reduce the gap in understanding different cases observed in the vascular adaptation.

Contents

List of Figures

List of Tables

Chapter 1

Introduction

In 2009, cardiovascular disease was the underlying cause of death accounted for 34.1% (871,517) of all 2,371,000 deaths in the United States [1]. Estimated expenditures for cardiovascular care in 2007 are estimated to exceed $431 billion. Surgical revascularization using autologous vein also remains a frequent used treatment option whereas 427,000 coronary bypass procedures had been performed in 2004 [4]. An increase in the rate of obesity and diabetes in the United States also suggest substantial increase in the need for these interventions over the next decade. Although there is a high demand often for these life-saving procedures, their medium- and long-term durability is not persistent as well. Since many technical approaches for improved patency have been exhausted, the recent belief has been that the future of enhancing the durability of these constructions relies in a better understanding of the biology of the vein graft wall.

The vein grafts are composed of three regions as lumen, intima and media (Figure

1.1a) at the time of implantation. There are boundaries between the intima and media and the external surface of the media, known as the internal elastic lamina (IEL) and external elastic lamina (EEL) respectively, which are a sheet of connective tissue. Inconsistent growth or shrink of these three regions play the most significant role in the vascular adaptation.

Vascular adaptation following local injury occurs through a combination of lumen narrowing (intimal hyperplasia) and wall (inward/outward) remodeling [5]. Over the past two decades, researchers have applied a wide variety of techniques to understand neointimal hyperplasia and vascular remodeling in an effort to identify novel therapeutic strategies ref [6–13]. However, despite incremental progress over these decades, specific cause/effect links between hemodynamic factors, inflammatory biochemical mediators, cellular effectors, and vascular occlusive phenotype remain unknown. Our hypothesis is that the complex interplay between monocyte biology, local vascular hemodynamics and the intrinsic wall milieu determines the course of vascular adaptation, leading to success or failure following the intervention. We propose here a computational framework to develop a hybrid agent-based model of vascular adaptation following acute intervention.

Our model is consistent with multiple scales in space and time. The continuous mechanic description of flow and tissue deformation incorporates at the time scale of second. The spatial resolution is relevant with the density of material, i.e., millimeter scale. The tissue plasticity is consistent at the spatial scale of the individual cells, i.e., micro meter scale. The time scale of tissue adaptation evolves with the order of the cell cycle expressed in hours. We have used separated and weakly coupled modules to

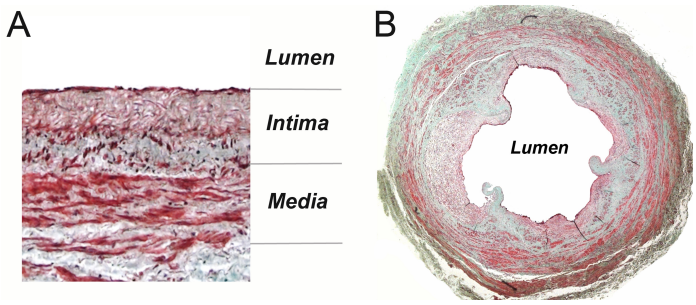

Figure 1.1: Histomorphology of a vein graft at implantation (a) and at six months post-implantation (b). [1]

approximate each scale. The coupling among these modules explain the relationship between tissue plasticity at the cellular level with environment conditions.

Our implementation is modular, which facilitates the agile development of the model and starts from the basic mecano-biology principle at the cell level. This implementation will help the theoretician and experimentalist by constructing different hypothesis and then testing with different sets of input parameters. It also serves as an analysis tool for the computational scientists and surgeons, where they can use this framework to update, modify and verify their hypotheses and experiments. The modular nature of our implementation provides an efficient agile development of this computational tool, which keeps the research process ongoing in the course of time. We would like to introduce our framework from the medical challenge at first, then the description of each module in our framework and the most significant parameter sets in our model and the procedure to identify them. Finally, we will present the interesting patterns generated by our framework efficiently with respect to computational time.

1.1 A short review

The hallmark of vascular occlusive disease is the specific localization patterns and focal nature of the disease process (Figure 1.1b). Based on morphologic and mechanical studies, arterial adaptation to altered shear stress encompasses two distinct processes; intimal hyperplasia and wall (inward/outward) remodeling [14]. The migration of smooth muscle cells (SMC) into the intima with the proliferation and deposition of extracellular matrix (ECM) defines the characteristics of Intimal hyperplasia; resulting in narrowing of the arterial lumen (Figure 1.1b). On the other hand, the preservation or loss of lumen area through reorganization of the cellular and extracellular components within the media, plays the most significant role in remodeling. From the surgical outcome, it is observed that the long term patency of vein graft implantation can be achieved through the modulation of the mediators that control the balance between these two processes [15]. The acute transposition of a vein segment from a low pressure and flow environment to the high pressure and flow arterial system leads to significant structural changes within the wall. These changes are characterized by an increase in intimal and medial thickness, which lead to the burst of smooth-muscle cell proliferation with conversion from a contractile to synthetic phenotype and the extracellular deposition of type I collagen and proteoglycans [16]. These early events in vein graft adaptation frequently continue in an uncontrolled manner, which leads to severe lumen narrowing and subsequent graft failure. Recent research results from ref [17–19] suggest that the reductions in local wall shear have been demonstrated to be critical components leading to accelerated intimal hyperplasia development, limited outward remodeling and vein graft failure.

Researchers for several decades have been trying to elucidate this connection between shear stress and vascular remodeling. From in vitro studies, it has been demonstrated that the genes important to vascular endothelial physiology such as nitric oxide synthase (NOS), endothelin-1, fibroblast growth factor (FGF), platelet-derived growth factor (PDGF), thrombomodulin are all influenced by the direct action of shear stress on endothelial function ref [20–22]. Several candidate of shear stress sensors in endothelial cells have been postulated, which include integrins, ion channels, G proteins and MAPK coupled receptors. Acting through a shear stress responsive element, consisting of a 6-bp core element (GAGACC) in many promoter regions, NF-B, AP-1, Sp-1, and Erg-1 can be activated by changes in the shear stress ref [20–22]. Work in our laboratory has been focused on identifying the key signaling pathways that control vascular remodeling in intact vasculature. While we have identified a handful of mediators (TNF, IL1, MMP-2) [20] to be regulated by flow during early vein graft adaptation, inhibition of these mediators has failed to influence this response significantly. Further underscoring this observation is the recent microarray studies performed in our laboratory, where the vein grafts exposed to divergent shear stress, was analyzed for their gene expression patterns. Two central questions regarding occlusive adaptations (inward remodeling and intimal hyperplasia) following vascular intervention remain unanswered:

Why does only a subset of patients following vascular injury demonstrate pathologic occlusive adaptations leading to lumen narrowing and failure of the intervention, while other patients undergoing the same therapy exhibit a favorable vessel wall healing response and preservation of the lumen?

Why is there substantial regional heterogeneity in vascular repair, such that focal regions of the vascular wall demonstrate advanced occlusive adaptations while neighboring segments are essentially free of disease?

Based on our ongoing investigations, we have hypothesized that the impact of shear stress on vascular adaptation to be more complex than can be described through a limited set of key (i.e., cytokine or signaling mediators). Instead, we present the evolving concept that the physical and biological environments are implicitly linked and lead to specific vein-graft phenotypes. Through the sequential process of model development and refinement, the complex relationships between the physical environment and the resulting graft morphology will be characterized. This leads to the development of a framework to understand vascular adaptation using different modules as we will explain in the following sections.

1.2 Scope and organization

In this subsection, I would like to summarize the contents and organizations of my dissertation briefly. There are four main sections; each divided into different subsections. The first section introduces the problem domain; our goal and strategy. The second section advances with our strategy to solve the problem; i.e., framework development; the modules of the framework and their descriptions mainly. The third section focuses on the scope of the framework to understand the formation of different patterns of the vein graft. We have introduced comparative analysis along with graphical presentation to explain our research findings. Finally, the last section represents the computational and high performance computing aspects of the framework.

Chapter 2

Framework and Modules

In this section, we will follow up with the modules of the framework. We have already explained in the previous section that the cells inside the vein graft go through apoptosis or mitosis affected by the shear stress and tension at the wall. As a result, there are three main modules here. The agent based module (ABM) explains the cellular activities i.e., the probability of cell apoptosis/mitosis, cell rearrangement after apoptosis or mitosis etc. Shear stress and tension can be explained using partial differential equations (PDEs). So our computational framework uses then a hybrid model that combines ABM and PDEs. The development of the framework followed by some hypotheses as we will follow up in the following sections.

2.1 Hypothesis used to generate the framework

Our hypothesis is based on two simple feedback mechanism (F1, F2) driven by the blood flow velocity and intramural pressure that compete with wall remodeling to support the phenomenological description accumulated from years of experiments - see Figure 2.1. This table helps to understand the vein graft adaptation associated with shear stress from heuristical and experimental perspective. A scale ranging from -5 to 5 is used to represent a reduction or increase in the parameter (i.e., intimal thickness), respectively.

	Day 1		Day 2 to 7		Week 2 to 4		Month 2 to 3		Long-term	
	Reduced Shear	Elevated Shear	Reduced Shear	Elevated Shear	Reduced Shear	Elevated Shear	Reduced Shear	Elevated Shear	Reduced Shear	Elevated Shear
Intimal Thickness	0	0	0	0	2	1	4	2	5	3
Medial Thickness	0	0	0	0	2	2	4	4	5	5
Outside Radius	0	0	0	0	1	2	3	4	4	5
Smooth Muscle Cell Proliferation	-4	-4	5	3	3	2	1	1	1	1
Matrix Content - Collagen	0	0	0	0	3	2	5	3	2	1
Matrix Content - Proteoglycan	0	0	`	3	2	1	1	0	0	0
Macrophage Content	0	0	5	3	3	2	1	0	0	0

Figure 2.1: Biologic Processes in the Vein Graft Adaptation [2].

(F1) Low shear stress promotes SMC division in the intima, which narrows lumen and gives intima thickening. As a result, it increases flow and shear stress.

(F2) High tension promotes SMC division in the media, which leads to wall thickening. As a result, this lowers the tension, if the difference between the internal and external pressure stays constant.

These two feedback mechanisms are nonlinear [2] and dependent on the inflammation. Inflammation triggers monocytes recruitment at the wall. As a result, this transforms into macrophage inside the wall. This may trigger SMC cell division and

cell apoptosis may promote inflammation, vice versa [9]. Additionally, when shear stress and tension are large enough, apoptosis may take over cell division [13].
The vein graft goes through local and global adaptation associated with the shear stress and tension as well. For example, when a carotid lumen gets narrowed with a stenosis, the adaptation mechanism is such that the reduction of resistance to flow downstream to compensate for some of the blood flow, decays through the vein graft. Additionally, some of the blood flow may be rerouted to other carotid by the mechanism. As a result, a thorough investigation of various scenarios is necessary to explain a potential spectrum of response of the vein graft.

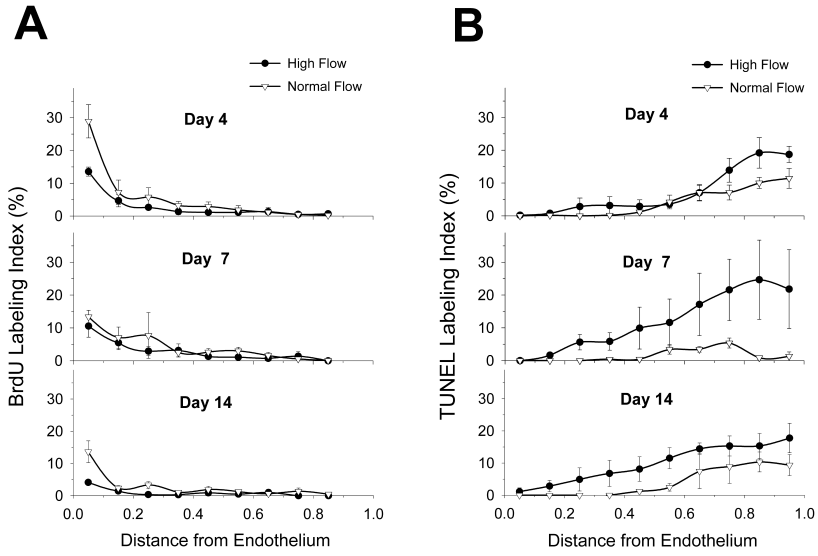

Figure 2.2: Spatial distribution of cell proliferation and apoptosis in rabbit vein grafts [3].

We have analyzed our rabbit model of shear-modulated vein-grafting adaptation Ref [21–24] to understand the response of the vein graft under different biologic

processes. The vein grafts were implanted into the arterial environment and observed either in low or high shear conditions (Figure 2.2). The spatial distribution of cell proliferation and apoptosis in the rabbit vein graft was observed using Bromodeoxyuridine (BrdU) incorporation and terminal deoxynucleotidyl transferase (dUTP) nick end labeling (TUNEL) assays ref [24, 25].From both Bromodeoxyuridine(Brdu) and Tunnel experiments, we find that the the injury at the wall (and EEL)is the main time dependent factor and somehow related to the production of macrophage and (MCP1, CCR2, with some delay). Since the vein graft tissue gets repaired in the course of time, we assume a very fast dynamic for cell mitosis that decays in time. Cell mitosis rate in the intima has the following assumed formula -see Figure 2.2:

rate of mitosis = function of (time) x exp(-Shear/dist to lumen) x function of (Shear).

Similarly cell mitosis in the media has the following assumed formula - see Figure 2.2:

rate of mitosis = function of (time) x function of (Tension).

Eventually, the transfer of biochemical components and migration of cells through the elastic membrane that separate the intima from the media, couple these two subdomains. As a result, this coupling mechanism requires some sets of rules describing the cellular activities associated with shear stress and tension in a spatial grid of cell sites, which can be explained with the agent based model (ABM) as we will follow up in the next section .

2.2 Agent-Based Module (ABM)

The ABM is well suited to describe the tissue at a cellular level. This bottom-up approach provides the foundation of a framework for the implementation of biological rules that can be explicitly tested using experimental models [3]. On the other hand, Parial Differential Equations (PDEs) are well suited to describe stress-strain relationship that defines the environmental condition in our problem. As a result, our current approach corresponds to a hybrid computational framework that integrates both ABM and PDE approaches. The ABM is responsible for the cell dynamic, i.e., SMC division and apoptosis as well as the ECM production/degeneration by SMC. This simplest uniform description is in fact a Cellular Automata (CA) [36]. CA consist of a spatial grid of sites that can take a finite number of discrete values, for example 0 and 1. Each CA site can evolve in discrete time as a function of the values in its nearest neighbors. We would like to start explaining ABM in one dimension at first for better understanding and then illustrate in two-dimensional spaces.

2.2.1 One-Dimensional Uniform Cellular Automata Model

We assume a one-dimensional line of CA sites; bounded by the lumen of radius R_{lumen}.The EEL is denoted as L_{EEL}.

The time scale is in hour. The algorithm scans each CA site in random spatial order each hour to decide on their eventual change of state according to the CA rules that we will define below.CA sites are either SMC or ECM. We seed a priori SMC and ECM in random order with a prescribed proportion θ that is a fixed number in (0,1) (Figure 2.3).

All CA rules below will come with probabilities. The model is then stochastic and we should always present statistical results based on many simulations starting from the same parameter set.

• **SMC dynamic** : SMC goes through division or apoptosis with periodicity T_{cell} = 12 hours. We choose a priori two parameters ($0 < P_{apoptosis}$, $P_{division} < 1$)for the probability law that drives this cellular process. We start with an initial random distribution of SMC with initial clock randomly generated in the (0, T_{cell}) interval. There is no synchronization between SMC and the number of cell event varies from one time step to the next one.

Every hour the algorithm checks the internal clock t^n of the SMC. We use the notation $a|b$ for a couple of integers (a,b) to say that a divides b.

If $T_{cell} \mid t^n$, then the cell may change state: we generate a random number $p = rand(1)$ in (0,1).

If $p < P_{apoptosis}$, then the cell goes to apoptosis and disappears from the line of ABM sites. Since there is no empty space possible for the two neighbor ABM sites to reconnect.

If $p > 1 - P_{division}$, then the cell divides and we add in its neighborhood a new cell that expands the line of ABM sites by one unit. The internal clock of the SMC and its daughter is reset to 0 otherwise, we just increment the clock of the cell by one unit.

We define d_{SMC} as the dimension of an SMC in the line of ABM sites and use d_{SMC}= 1.

Because the ABM is a uniform one-dimensional structure, it is easy to provide an Ordinary Differential Equation (ODE) that describes the population of SMC. Let Y^n_{SMC} be the total amount of SMC in the ABM line of sites at time t^n (n stands for the time step expressed in hours). We have

$\frac{\partial Y_{ECM}}{\partial t_c} = (P_{production} - P_{degradation})\, Y_{SMC}$, (1)

where t_c is the time scale of division. Obviously, equilibrium corresponds to

$P_{apoptosis} = P_{division}$ (2).

Anything different from (1) and (2) leads to extinction ($P_{division} < P_{apoptosis}$) or exponential growth ($P_{division} > P_{apoptosis}$)in this rather simplified model.

• **ECM dynamic** : ECM is either produced or degenerated by SMC. This process occurs at a different time scale T_{matrix}. Typically, $T_{matrix} << T_{cell}$ and $T_{matrix} = 2$ hours. We assume that ECM does not transform itself or move. Actually, the spatial

matching of ECM into ABM units is driven by how much ECM can be produced by an SMC into T_{matrix} hours. The model uses three new parameters ($P^*_{production}$, $P^1_{degradation}$, $P^2_{degradation}$)to drive the dynamic of the SMC−ECM interaction.

The production of an ECM by an SMC is as follows: every time $T_{matrix} \mid t^n$, we generate a random number p = rand(1) in (0,1).

If $p < P^*_{production}$, then the cell produces an ECM unit and we add in its neighborhood a new ABM site corresponds to this new ECM contribution. The probability that an ABM site contains an ECM unit disappears by degradation depends on the number of SMC neighbor surrounding that ECM site as follows:

$$P^1_{degradation} = P^*_{degradation}, P^2_{degradation} = 2P^*_{degradation}. \quad (3)$$

Figure 2.4 shows an illustration of the ABM output after few hours.

In this model ECM has no effect on SMC population besides allowing migration. The ODE model describing the population dynamic of ECM is as follows:

$$\frac{\partial Y_{ECM}}{\partial t_c} \cong (P^*_{production} - P^*_{degradation})\, Y_{SMC}, \quad (4)$$

assuming that the population of SMC is stable, we keep the proportion of SMC versus ECM stable if the number of ECM degradation balances the number of ECM production. This is an approximation because all these events are not a priori independent:

$$(1-\theta)[\theta^2\ 2\ P^*_{degradation} \ +\ 2\theta\ (1-\theta)\ P^*_{degradation}] = \theta\ P_{production}. \quad (5)$$

The above rule gives

$$2\ (1-\theta)\ \ P^*_{degradation} \ =\ P_{production}. \quad (6)$$

We have seen that SMC can go either through exponential growth or extinction if (2) is not satisfied. Because of the one way coupling between the dynamic of SMC and ECM, once an SMC disappears, the population of ECM remains identical for the rest of time.

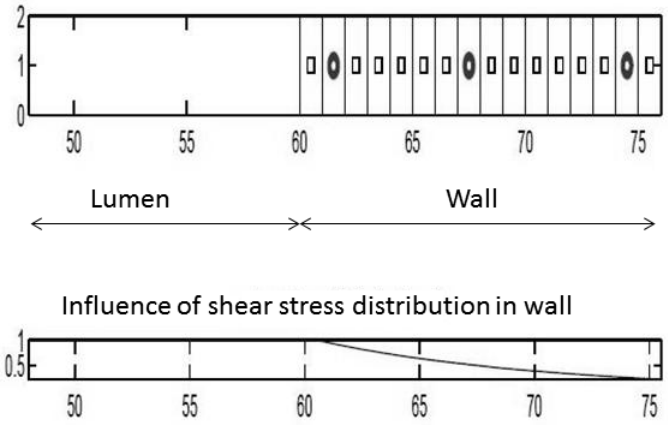

Figure 2.3: Initial distribution of SMC (circles) and ECM (squares).

This model is driven by the following 4 parameters:

$$0 < P_{apoptosis}, P_{division}, P^*_{production}, P^*_{degradation} < 1. \quad (7)$$

As discussed earlier, we expect the system to have asymptotically constant population of SMC and ECM if (2) and (6) are satisfied. We will define that solution

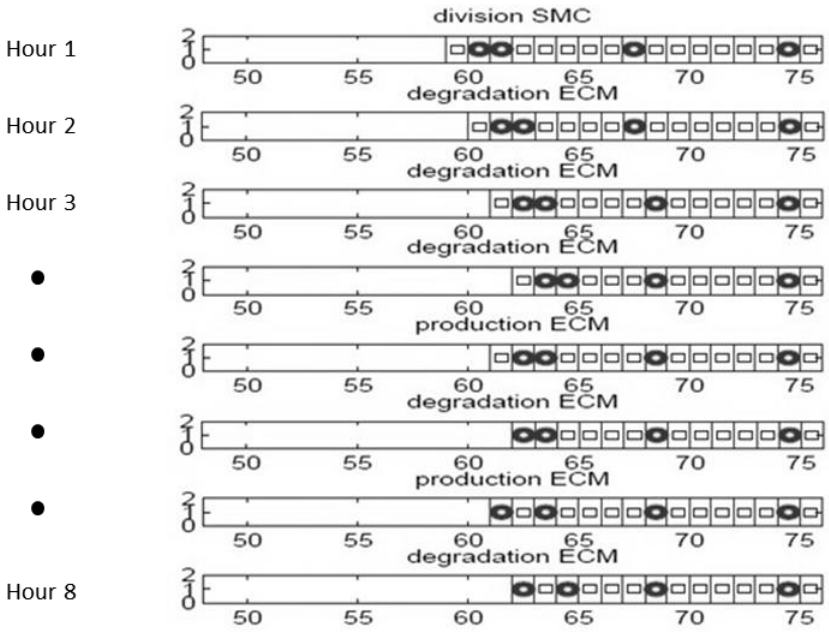

Figure 2.4: Sequence of SMC/ECM apoptosis/mitosis.

as the basic solution. We are going to produce a minimum new set of mechanical environment dependent rules in the ABM to support the phenomenon observed in the experiments with the rabbit vein graft.

2.2.2 The Coupling of ABM with Environmental Conditions

The rules of the ABM are as follows:

1. All the probability rules will deviate from the equilibrium relation:

   $$P_{division} = P_{apoptosis}, \quad \beta P^*_{degradation} = P_{production}. \quad (8)$$

   where β is adjusted numerically to provide a "basic solution" such that in the absence of the influence of any mechanical parameters, this solution keeps asymptotically the same number of SMC/ECM in each layer (see Appendix). The basic solution is governed by two parameters:

   $$P_{division} = \alpha_1 > 0, \; P_{production} = \alpha_2 > 0. \quad (9)$$

   These two parameters should be adjusted to match the time scale of cell division and extracellular matrix deposition respectively.

2. All the probability rules are weighted by a time factor that mimic the macrophage activity:

   $$A(t) = \exp -(\tfrac{t-T_i}{\delta T_i})^2. \quad (10)$$

   As noticed from Figure 2.1, the macrophage contains growth to reach its maximum around time T_i and the decay with time scale δT_i. This rules gives two parameters:

   $$T_i = \alpha_3 > 0, \; \delta T_i = \alpha_4 > 0. \quad (11)$$

   The ABM rules depend on mechanical environment quantities and this introduces the influence of spatial location and layer type. We will denote $\Delta\tau$ as the

deviation from normal shear stress condition (i.e., $\delta\tau = \tau - \tau_0$.) Similarly, we will use $\Delta\sigma$ for tension. We will denote $\bar{\tau}$, $\bar{\sigma}$ as a fixed reference value for shear stress and tension respectively and they are used to normalize these quantities.

3. The position of internal elastic lamina is driven by a one way flow of SMC in the lumen direction. The probability of an SMC crossing the IEL is

   $$P_{through} = \alpha_5 A(t)\,(1 + \alpha_{13}\Delta\tau(y)/\bar{\tau})\,(1 + \alpha_{14}\Delta\sigma_r(y)/\bar{\sigma}),\ \alpha_5 > 0. \quad (12)$$

   Initially, we assume arbitrarily that we have 3 cells in the intima, which is realistic for the rabbit experiment.

4. Cell division in the intima is influenced by the growth factor that have an exponential decay in the intima, but regulated globally by the shear stress:

   $$\Delta\tau(y) = \Delta\tau_{wall}\ \exp(-\tfrac{y-R_{lumen}}{\alpha_8\, d_{SMC}}), \quad (13)$$

   $$P_{division} = \tfrac{1+\alpha_6\,\Delta\tau(y)/\bar{\tau}}{1+\alpha_7\,\Delta\tau_{wall}/\bar{\tau}}. \quad (14)$$

   and in the media:

   $$P_{division} = \alpha_1 A(t). \quad (15)$$

5. Cell apoptosis is regulated by the radial stress in the media. In the intima:

   $$P_{apoptosis} = \alpha_1 A(t) \quad (16)$$

   and in the media:

   $$P_{apoptosis} = (1 + \alpha_9\ \Delta\sigma_r(y)/\bar{\sigma}). \quad (17)$$

6. Finally, we will assume that ECM degeneration is regulated by the shear stress in the intima, and tension in the media in the same abstract form. In the intima:

$$P^*_{production} = \alpha_2\ A(t), \quad (18)$$

$$P^*_{degradation} = \alpha_2\ A(t)\ (1\ +\ \alpha_{10}\ \Delta\tau(x)/\bar{\tau}). \quad (19)$$

and in the media:

$$P^*_{production} = \alpha_2\ A(t), \quad (20)$$

$$P^*_{degradation} = \alpha_2\ A(t)\ (1\ +\ \alpha_{11}\ \Delta\sigma_r(y)/\bar{\sigma}). \quad (21)$$

It should be noticed that this set of axioms does not impose which factor up-regulate or down regulate SMC and ECM dynamic, because the vectors of parameters $(\alpha_5, \alpha_6, \alpha_7, \alpha_8, \alpha_9, \alpha_{10}, \alpha_{11}, \alpha_{12}, \alpha_{13}, \alpha_{14})$ have no predefined sign. Besides these, all rules compute a deviation from the basic solution. For example, this rule does not express a true rate of SMC division, ECM production, which is not needed. We rather focus on the differences in the rate of gain or lost that is $(P_{apoptosis} - P_{division})$ and $(P^*_{production} - P^*_{degeneration})$. A rather simplified one dimensional model was tested against our experimental data [47] extensively. However, the result was noisy, since the small number of SMC and ECM in this one-dimensional model was very small to replicate the experimental data. As a result, we would like to move on with a two-dimensional model, which we will follow up in the next subsection.

2.2.3 A Two-Dimensional Model

We will explain the ABM in two-dimensional spaces here. We can even validate the model using the histology data coming from the cross section of the vein graft. The two-dimensional model uses a hexagonal grid of sites divided into three regions; lumen, intima and media (Figure 2.5). The algorithm has the main parameter framework as it is above. We would like to introduce the main modification in the algorithm (Figure 2.6) here.

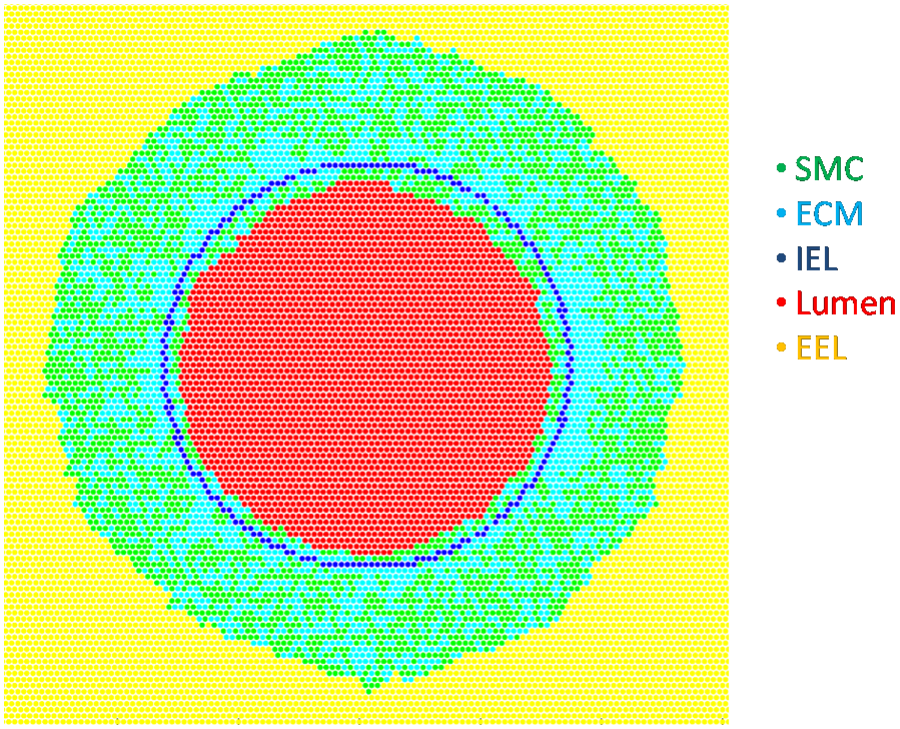

Figure 2.5: Two dimensional hexagonal grid of sites.

• In two-dimensional spaces, there is no unique solution to rearrange the sites of ABM after an SMC/ECM forms or disappears, because there is a fixed hexagonal grid for our ABM. Existing models of cell-cell contact interaction have a high level

of uncertainties and are difficult to calibrate in practice. Our assertion is that this reorganization on a regular ABM grid should correspond to some minimum of mechanical energy required to move the SMC and ECM of the ABM's representation of the tissue. We will assume that the new cell (after mitosis), or matrix element (after deposition) pushes its surrounding elements in the ABM along the shortest path that leads to an empty space (Figure 2.7). This solution minimizes the number of SMC/ECM moves on the hexagonal grid.Vice versa, the empty site left by the apoptosis of a cell or the degradation of a matrix element, gets filled by its surrounding elements in a way that leaves no cell empty along the shortest path to an empty space. It is expected that this reorganization in the tissue might be trapped by some local optimum minimum path. We introduce some noise in the searching algorithm so that the founded path is close to the minimum path, but may not necessarily be the absolute global optimum one.

• In the two-dimensional space model, as opposed to the one-dimensional case, we should have motion of cells at the interface of the lumen or at the interface with the vein graft's surrounding. We should move SMC/ECM at those sites next to these interfaces that systematically increases contact surface between SMC/ECM elements (Figure 2.8). This motion is applied at each time step of the algorithm, i.e., every hour. However, we observe in our simulation that this local procedure does not preserve the circular shape of the interface as expected resulting in the growth of some mushroom like structure that are not realistic; in particular for the external wall.

For the external wall, we assume that the surrounding tissue applies some positive

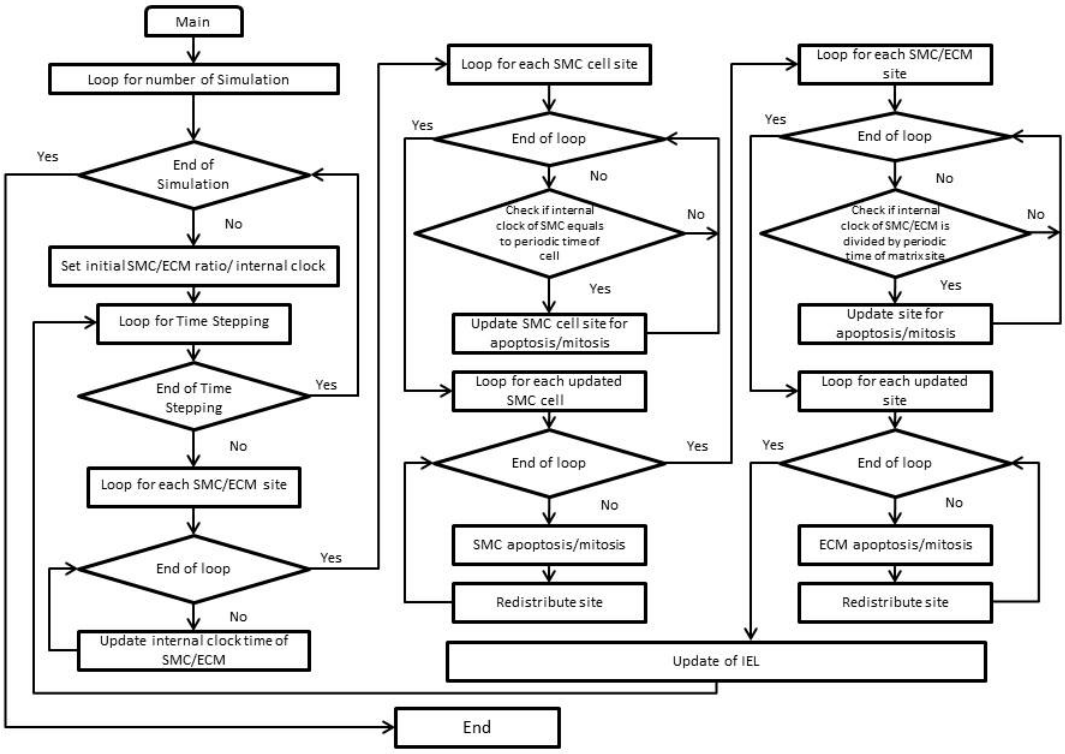

Figure 2.6: Flow diagram of two dimensional model.

pressure on the outside wall toward the graft center. Consequently, SMC/ECM may move toward sites that are closer to the center of the graft or increase contact. Similarly, for the lumen wall, we can assume that the flow applies some positive pressure in the opposite direction as above. This mixture of both rules keeps the vein graft getting closer to a cylinder depending on the weight of each rule and the number of cell migration allowed at each time step.

The probability rule on ECM degeneration in the two-dimensional case must be revisited: in the one-dimensional case, the probability of ECM degeneration is

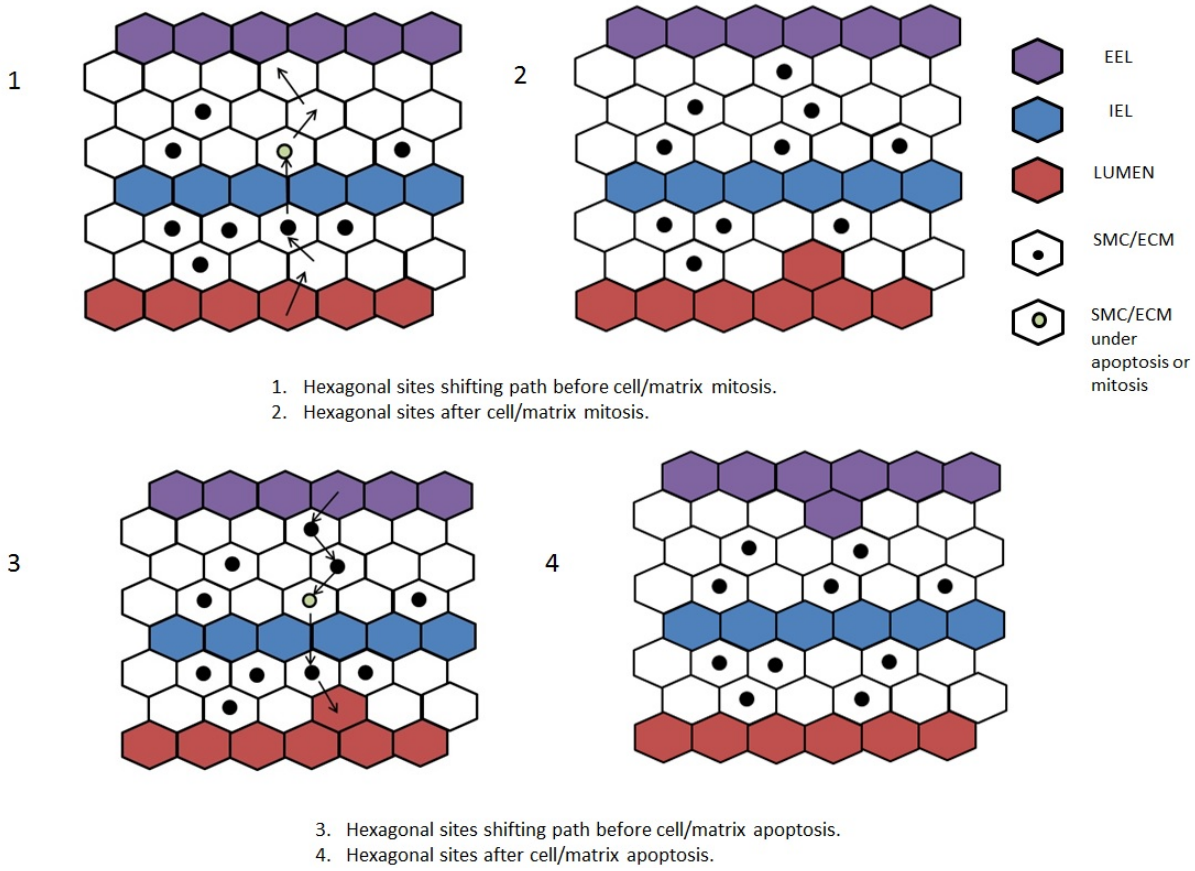

Figure 2.7: Management of the tissue remodeling on the fixed hexagonal grid.

proportional to the number of SMC in its neighbor. In the two-dimensional case, an ECM element can have up to six SMC neighbors. From our numerical observation with the two-dimensional basic solution, we found that SMC has the tendency to form cluster of cells: ECM inside such cluster gets removed. To keep an even distribution in space for ECM, we have imposed a limit of maximum number of SMC surrounding an ECM. The probability for an ECM to be degenerated by an SMC is proportional to the number of SMC neighbors up to two. Above a number of two SMC neighbors, the probability of matrix degeneration is kept the same. This rule is completely

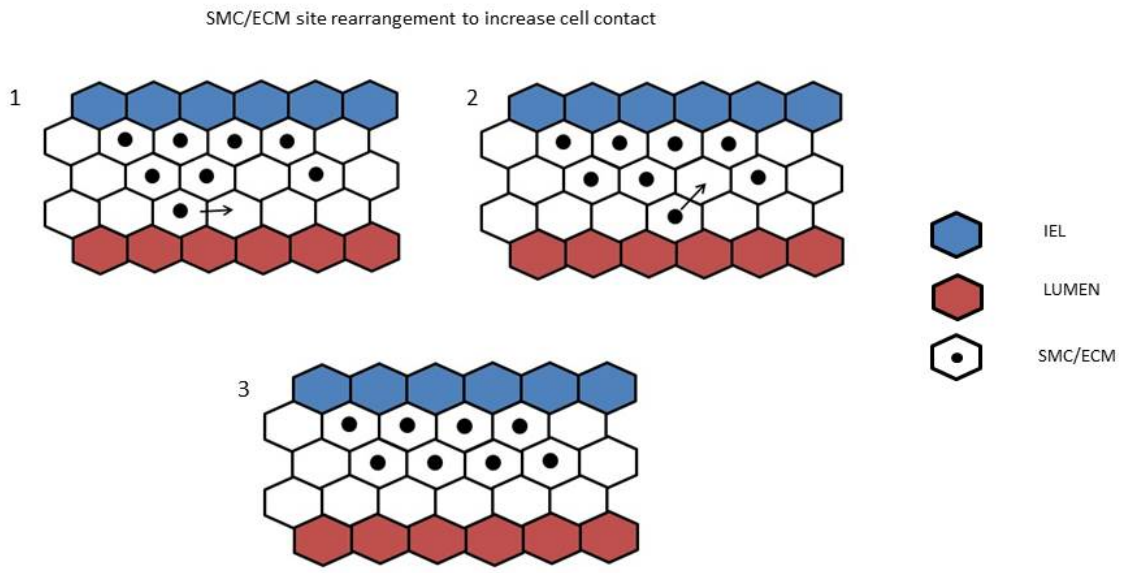

Figure 2.8: Motion of an SMC on the hexagonal grid at the lumen wall.

heuristic and motivated by the observation of an "emergent property" of the ABM.

• In the one-dimensional case, the IEL is defined to be one specific ABM site's location. SMC can simply migrate from the media to the intima through that interface. For the simplicity of implementation, we have assumed that the IEL stays close to a circle and is approximated by an averaged radius. In two-dimensional spaces, the growth and shrink of the IEL depends on the shear stress generated at the lumen wall. We have introduced a parameter,α_{15} to explain this. The probability of

growth is proportional to the increase of shear stress and vice versa, the probability of contraction is proportional to the decay of shear stress:

$$P_{outward/inward} = \alpha_{15} \frac{\Delta \tau_{wall}}{\bar{\tau}}. \quad (22)$$

Occasionally, if the average displacement is larger than half a site diameter or the standard deviation is more than a cell, we reset the lamina sites on the grid to be a circle defined by the mean radius of the previous quasi circle.

So far we have explained the ABM in two-dimensional spaces completely. In the next subsections, we would like to explain the mechanical model that provides environmental conditions to the cells.

2.3 Blood Flow Module

In this subsection, we would like to explain the calculation of shear stress inside the lumen wall ($\partial\Omega_{lumen}$). We use a diffusion operator (Figure 2.9) inside the tissue wall to compute the shear stress induced growth factor (G).

$$\frac{\delta G}{\delta t} = \Delta G; G_{\partial\Omega_{lumen}} = \tau, \quad (23)$$

where G is discretized with the P1 Finite Element associated to the hexagonal grid:

$$G^i_{n+1} - G^i_n = \sum_{j=j_1}^{j_6} G^j_n - 6G^i_n; n\epsilon(1, \alpha_8). \quad (24)$$

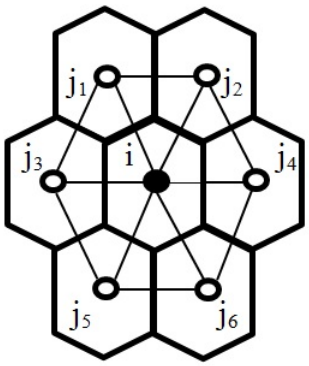

Figure 2.9: The calculation of the diffusion operator.

α_8 is now the number of time steps in an explicit diffusion process on the ABM's grid. The diffusion of growth factor depends on the convexity and curvature of the lumen wall and will be automatically enhanced or reduced versus the standard exponential decay in the normal direction to the wall based on this dependency. We

will explain the calculation gradually in the following.

The cross section of the lumen can have irregular shape. The time scale for tissue plasticity is so large compare to the 1Hz frequency of blood flow that we have assumed that the cells adapt to the average of the mechanical environment conditions. We assume that the error we do by neglecting the nonlinear convective term in Navier Stokes and using a steady flow, is somewhat smaller than the level of uncertainty we have on the biology. We use zero-velocity boundary condition at the wall ($\partial\Omega_{lumen}$) and the conservation of flux at the time scale of tissue plasticity, i.e.,

$$\int_{\partial\Omega_{lumen}} u dy dz \ = \ Flux. \quad (25)$$

We compute a steady potential flow inside the lumen driven by a constant pressure gradient $\frac{dP}{dx}$ (Figure 2.10). From that potential flow, we compute the normal shear stress component τ_{wall} at the wall. The set of equation of fully developed duct flow is

$$\frac{d^2u}{dy^2} + \frac{d^2u}{dz^2} = \frac{1}{\mu}\ \frac{dP}{dx} \ = \ C^t,\ u_{|\partial\Omega_{lumen}} = 0, \quad (26)$$

where μ is viscosity. To solve that problem, we compute the solution of the standard Poisson problem:

$$\Delta v(y,z) = -1, (y,z)\epsilon\Omega_{lumen}, v_{|\partial\Omega_{lumen}} = 0. \quad (27)$$

We have then: $u = C_0 v, \ (28)$ where C_0 is such that the flux is conserved.

We use a finite volume scheme to compute v on a regular spatial grid and an immersed boundary implementation of the no slip wall condition v=0 on $\partial\Omega_{lumen}$.

This potential flow should be computed however in the (deformed) geometry of the vein section that is deformed by the transmural pressure, i.e., the difference of

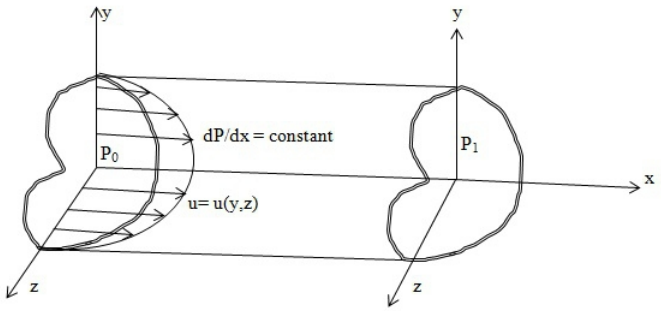

Figure 2.10: Steady potential flow.

pressure inside the lumen and the outward wall. The ABM in unloaded configuration serves as the reference position for all SMC/ECM dynamical changes. We should use the inverse map of the displacement (Figure 2.12) to retrieve the wall shear stress for the unloaded geometry. We have also verified the numerical approximation of shear stress with the analytical solution of shear stress (see Appendix). From Figure 2.11, it is evident that the numerical approximation of shear stress is consistent with the analytical solution.

In the next subsection, we would like to explain the module responsible for the calculation of the tissue deformation.

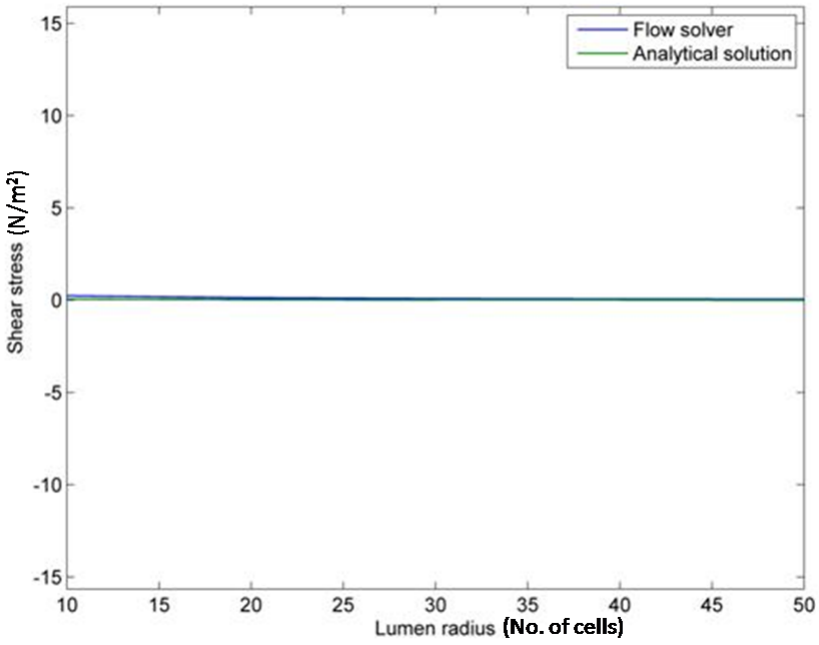

Figure 2.11: Shear stress VS lumen radius.

2.4 Tissue Mechanic Module

As explained in the previous section, the vein graft is deformed because of the transmural pressure (Figure 2.12). This transmural pressure generates tension at the wall, which is ultimately responsible for the division of SMC in the media. We would like to approximate this tension at the wall so that this can be applied to the ABM rules associated with tension.

We use a well-known Neo-Hookean hyperelastic model to simulate the tissue deformation of the vein wall generated by the transmural pressure. This material form of strain energy potential is given by:

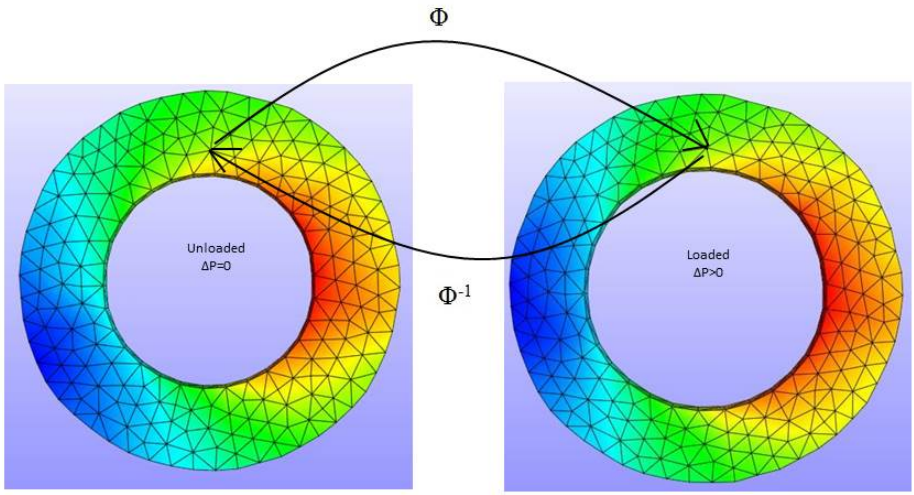

Figure 2.12: Tissue deformation (Different colors represent the variation of the tension).

$$W \;=\; \mu_1/2\,(J^{-2/3}I_1 - 3) \;+\; K/2\,(J-1)^2, \quad (29)$$

where W is the strain energy per unit of volume, I_1 is the first invariant of the left Cauchy-Green deformation tensor, μ_1 is the initial shear modulus of the material, K is the bulk modulus, and J is the determinant of the elastic deformation gradient. In this Neo-Hookean model, the solid parameters are represented by μ_1 and K. In equation (29), the first part, proportional to μ_1, is linked to the trace of the left Cauchy-Green deformation tensor. This term could be interpreted as quantifying the effect of stretch on the solid; whereas the second part of equation (29) gives K proportional to the determinant of the deformation gradient tensor, interpreted as

the quantification of any change in volume. Therefore an incompressible material will tend to penalize any change in volume of the solid. For this reason, one interprets the shear modulus and the bulk modulus respectively as the stiffness and the compressibility of the tissue.

The ABM model works on the unloaded model geometry. From the practical point of view, the ABM module generates the contour of the lumen (X_l, Y_l) and EEL (X_E, Y_E) in cell dimension. This is converted into a physical domain in millimeter scale. For the Finite Element simulation, the mesh of this two-dimensional ring shape domain is generated by Gmsh [36]. Gmsh is distributed under the terms of the GNU General Public License (GPL) and uses primarily a Delaunay triangulation.

This mesh is then passed to the finite element (FE) software Febio. Febio is an open source nonlinear finite element solver that is specifically designed for biomechanical applications [36].

Since we choose to work with a potential steady flow, we use a quasi-static method that neglect inertia terms. Febio calculates the FE approximation of the tension at each node of the mesh of the vein graft by using the following formula:

$$\sigma = \sqrt{[(\lambda_1 - \lambda_2)^2 + (\lambda_2 - \lambda_3)^2 + (\lambda_3 - \lambda_1)^2]/2}\,, \qquad (30)$$

where λ_i are the eigenvalues of the stress or strain tensor of each point of the node (each node has three points) in descending order. All of these calculations correspond to the boundary condition where Young modulus is 2000, poisson ratio is 0.49, shear modulus $\mu_1 = 3448$ Pa, bulk modulus K = 33333 Pa and internal and external pressure on the vein graft are 12.66 N and 12.00 N respectively [36]. This information needs to be passed back to the ABM in the unloaded coordinate system.

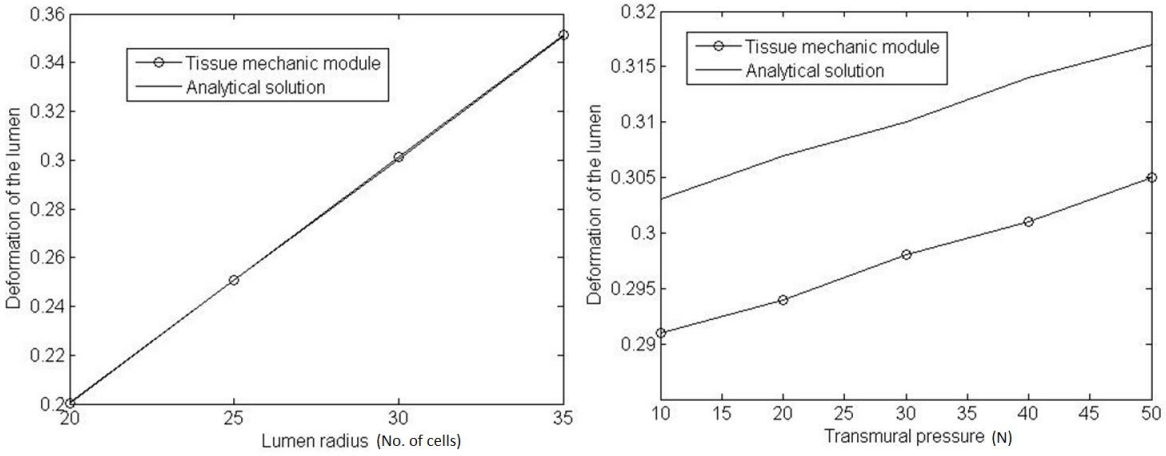

Figure 2.13: Verification of Tissue module.

To verify the tension approximated by the tissue mechanic module, we have compared the deformation of the lumen wall with different lumen radius and at constant lumen radius with different transmural pressure. From Figure 2.13, it is evident that the numerical approximation of tension is consistent with the analytical solution (Appendix). This concludes the description of tissue mechanic module. We would like to summarize the interaction among these three modules in the next subsection.

2.5 Coupling Mechanism

We already explained in the previous three subsections about the functionality of each module. At first, the ABM module passes the contour of lumen (X_l, Y_l) and EEL (X_E, Y_E) to the Tissue mechanic module. The tissue mechanic module returns the deformed shape of the vein graft(i.e., (X_l', Y_l') and (X_E', Y_E')) to the blood flow module and tension $\sigma(X_E'$, $Y_E')$ back to the ABM module. The ABM module then updates the number of SMC/ECM based on the probabilistic rules associated with $\sigma(X_E'$, $Y_E')$. The blood flow module calculates $\tau(X_l', Y_l')$ and $\tau_{wall}(X_E', Y_E')$ and returns this information back to the ABM module. The ABM module then updates the number of SMC/ECM based on the probabilistic rules associated with $\tau(X_l', Y_l')$ and $\tau_{wall}(X_E', Y_E')$ (Figure 2.14).

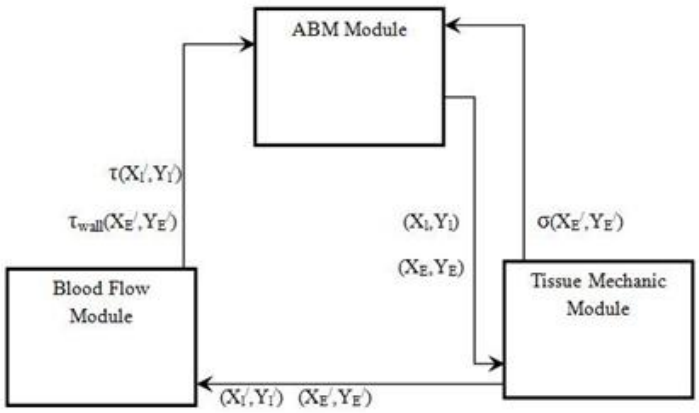

Figure 2.14: Coupling among three modules.

The data transfer between the ABM and blood flow module occurs through memory transfer, since the blood flow module is an independent module developed by

ourselves. On the other hand, the data transfer occurs through transferring files between the ABM and tissue mechanic module. It is because of the fact that the tissue mechanic module calculation incorporates two types of software (i.e., Gmsh, Febio) and these two softwares communicate through files between them.

Both the mechanical modules use the quasi steady approximation. The ABM module on the contrary is unsteady. The time scale is about an hour, which is appropriate to count for the cell cycle. The coupling algorithm is adaptive with respective to time. The ABM receives the shear stress and tension calculated by the two mechanical modules based on the change of number of cells/matrices. It occurs only when the lumen and the external wall of the vein graft in the ABM change position enough to lead to a change of number of cells/matrices to a few percent (i.e., 2%).

Let us consider that we can change anytime our basic potential flow solver by an off-the-shelf commercial code such as Fluent that provides a more realistic flow or update our soft tissue mechanic model with something that would be more specific to the vein wall composition. However as noticed earlier, we believe that most of the uncertainty in our model comes from the biological component, as noticed in the experimental measurements.

Chapter 3

Sensitivity Analysis and Pattern Formation

In this section, we would like to explain the sensitivity analysis of the ABM. There are two types of sensitivity analyses we have performed; local and global sensitivity. These sensitivity analyses will help us to determine which sets of parameters are the most significant in the vein graft adaptation. Then we can play with those significant parameters to generate interesting patterns found in the vein graft adaptation. Finally, we will cross validate our framework with some sets of differential equations explaining the vein graft adaptation.

3.1 Local Sensitivity Analysis

At first, we would like to understand the linear effect of the parameters on the number of SMC/ECM. We start with a linear sensitivity analysis around the basic solution state. This local sensitivity analysis presents the effect (deviation of mean, standard deviation from the basic solution) for a particular parameter of the mathematical model, keeping other values of the parameters fixed as it is for the basic solution. The linear sensitivity analysis of SMC/ECM apoptosis/mitosis is based on the following formula:

$$P = P_0(1 + \beta * \tau/\bar{\tau}), (31)$$

where P_0 is the initial probability of SMC/ECM apoptosis. The ratio of $\tau/\bar{\tau}$ is $\sim$ 1 (i.e., basic solution). $\beta = \alpha_5, \alpha_6, ..., \alpha_{14}$ and $\beta\epsilon(0, \beta_0)$ where β_0 is a value of β such that $(P - P_0)/P_0 \leq 10\%$. Equation (31) will let us test our model with the positive and negative perturbation of the parameters.

We have run the simulation with this parameter settings in parallel and found out that some parameters show linear sensitivity $\alpha_5, \alpha_7, \alpha_9$, while others not. We plot the positive (red bar in Figure 3.2) and the negative (green bar in Figure 3.2) perturbation of the parameters β versus the number of SMC/ECM with their standard deviation and find out the following main two characteristics:

• Local sensitivity with linear characterisitcs: The parameter α_5 shows linear effect (number of SMC/ECM increaes in the intima and decreases in the media) on the model as suggested by Figure 3.1. It is also sensitive as the mean and the standard deviation deviate from the basic solution (black bar). α_5 has only positive pertur-

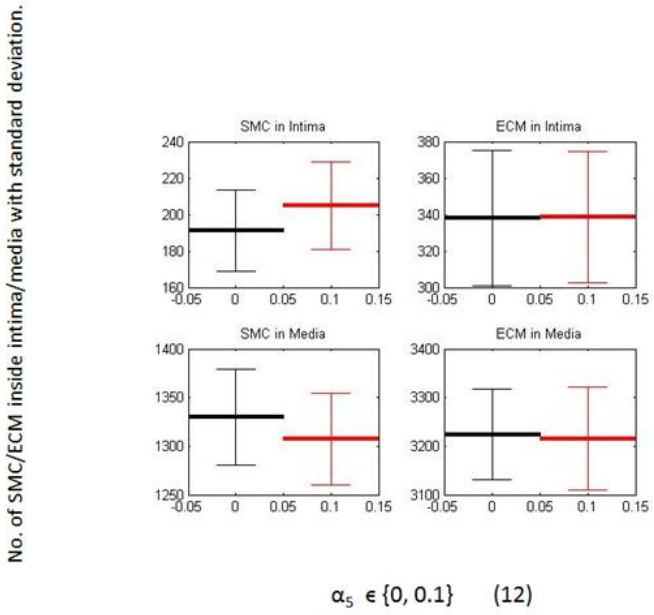

Figure 3.1: Linear sensitivity of α_5 (equation (12)).

bation as suggested by (12). An interesting feature of this linear sensitivity analysis is that SMC inside the intima increases, while in the media decreases as we apply positive pertirbation. On the other hand, ECM remains unchanged while we apply positive perturbation.

α_7 has positive and negative perturbation as suggested by (14). It is inversely associated with SMC division inside the intima and shows linear sensitivity of SMC/ECM inside the intima and media.

α_9 is positively associated with SMC division inside the media (17).So we find linear sensitivity inside the media here as suggested by Figure 3.3.

• Local sensitivity with nonlinear characteristics: There are other parameters, which do not show linear sensitivity rather nonlinear characteristics as suggested by Figure 3.4, 3.5, 3.6. It is evident from Figure 3.4 that the parameter α_{10} shows

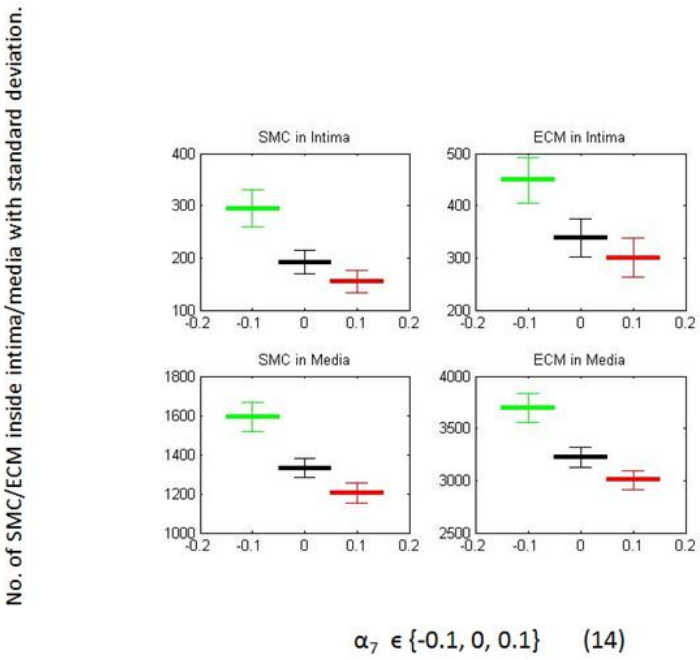

Figure 3.2: Linear sensitivity of α_7 (equation (14)).

nonlinear sensitivity in case of SMC/ECM inside the intima whereas α_{11} and α_{13} show nonlinear sensitivity in case of SMC/ECM inside the media (Figure 3.5, 3.6). This local sensitivity analysis determines the effect of individual parameter on the number of SMC/ECM. If we want to understand the effect of all the parameters, we have to perform global sensitivity analysis, which we will explain in the following subsection.

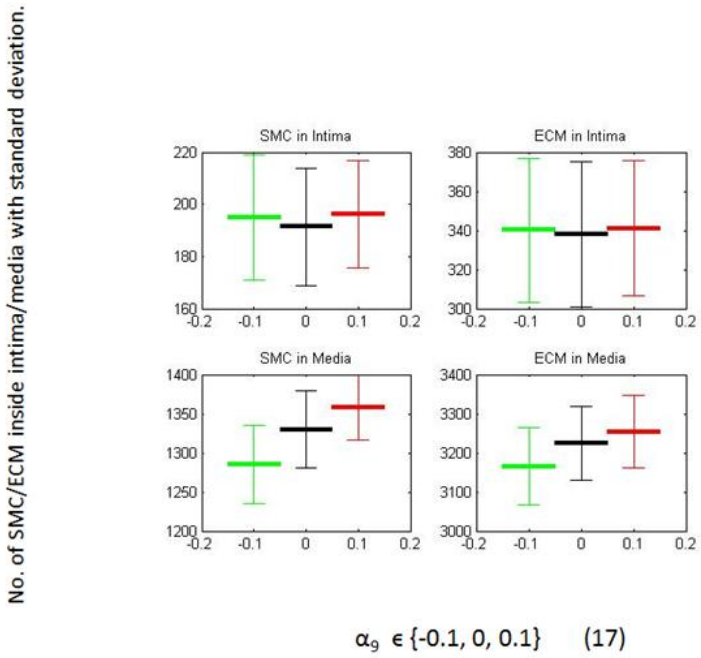

Figure 3.3: Linear sensitivity of α_9 (equation (17)).

3.2 Global Sensitivity Analysis

The global sensitivity analysis means to figure out the effect (deviation of mean, standard deviation from the basic solution) of changing the value of the parameters simulataneously of the model [48]. The objective of this kind of sensitivity analysis (SA) is to identify critical input (parameters and initial conditions) of a model and quantifying how the input uncertainty impacts the model outcome. There are several such techniques as monte-carlo (MC) approach, latin hypercube sampling (LHS), partial rank correlation coefficient (PRCC), extended fourier amplitude sensitivity test (eFAST). We have applied PRCC technique to understand the global sensitivity of the parameters as this method is being widely used in cell biology [35].

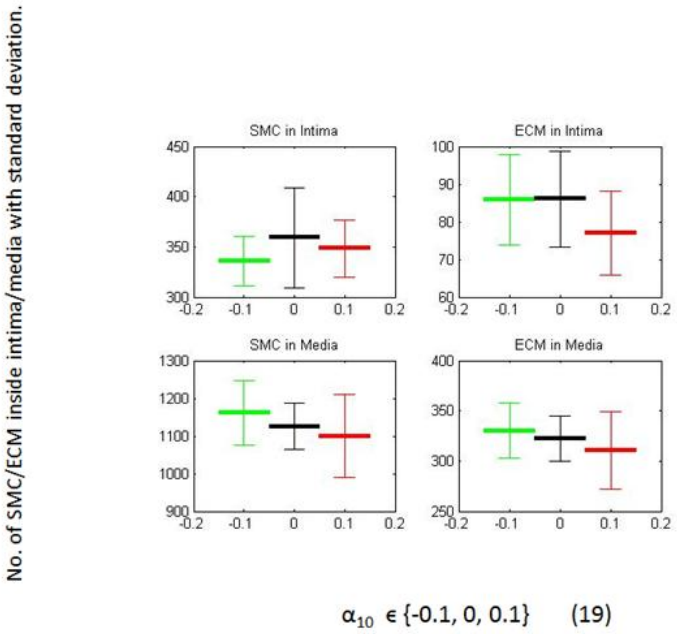

Figure 3.4: Nonlinear sensitivity of α_{10} (equation (19)).

The PRCC represents the partial rank correlation coefficient between the input and output variables. In PRCC calculation, the parameters have been uniformly sampled and then for each set of parameters, the simulation is run to generate the output (i.e., the number of SMC/ECM inside intima/media). Next,the input and output matrices have been rank transformed and then correlation coefficient (CC) has been calculated for each of the input to get the PRCC index [35]. This PRCC index can be positive or negative which means positive and negative correlation between the input and output respectively. As for example, in Figure 3.7, where we plot the PRCC indices for all the parameters, some parameters are positively correlated in case of SMC/ECM inside intima/media, whereas others are negatively correlated. The highest positive PRCC index of a parameter means that this parameter plays the most significant role in SMC/ECM production (i.e., α_6 in SMC production inside

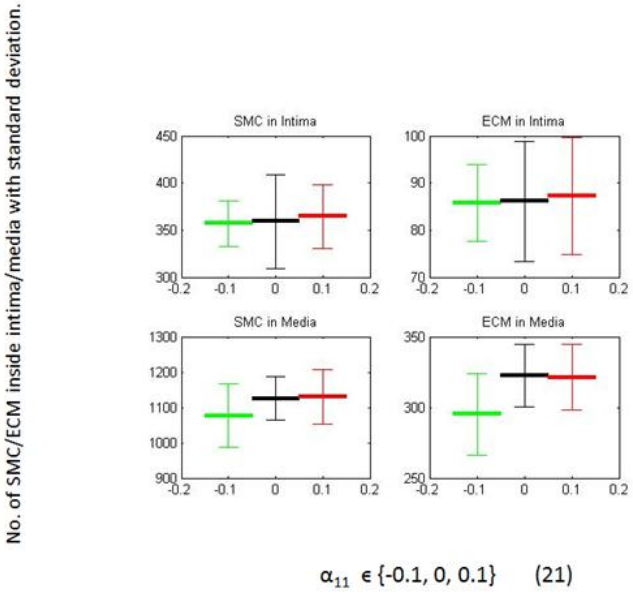

Figure 3.5: Nonlinear sensitivity of α_{11} (equation (21)).

the intima) and vice versa. This nonlinear sensitivity analysis definitely gives an idea about which sets of parameters are the most significant to generate interesting pattern observed in clinical histology.

As for example, α_6 is directly connected with the probabilistic rule of SMC generation inside the intima (15) and the PRCC index from Figure 3.7 also verifies this fact. We can also introduce variation in SMC generation inside the intima by using those parameters, which have negative PRCC indices. We can apply this observation from this nonlinear sensitivity analysis in the production or the degeneration of SMC or ECM inside the intima or media. This sensitivity analysis definitely gives the startup formation of generating interesting pattern found in the vein graft adaptation, which we will elaborate in the next subsection.

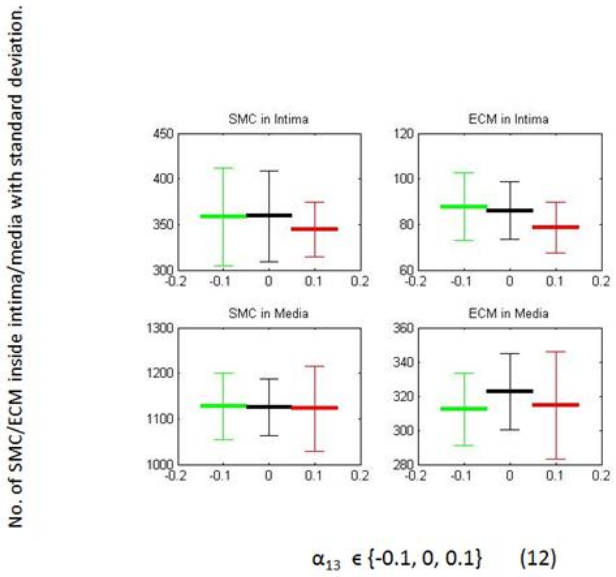

Figure 3.6: Nonlinear sensitivity of α_{13} (equation (12)).

3.3 Pattern Formation

We would like to explain the underlying principal of the formation of interesting pattern of the vein graft using our framework in this subsection. We will start from the results of clinical observations at first.

The vein graft shows two sets of interesting patterns (Figure 3.8) such as intimal hyperplasia and medial hyperplasia. Intimal hyperplasia is the result of the expansion of intimal region due to increasing number of SMC and ECM inside the intima. Medial hyperplasia is also the result of increasing number of SMC and ECM inside the media. Here we would like to explain how these two sets of patterns can be reformed using our framework started from the basic solution. We will also focus on other temporary patterns found in the vein graft implantation.

There are two feedbacks associated with the environmental conditions observed in

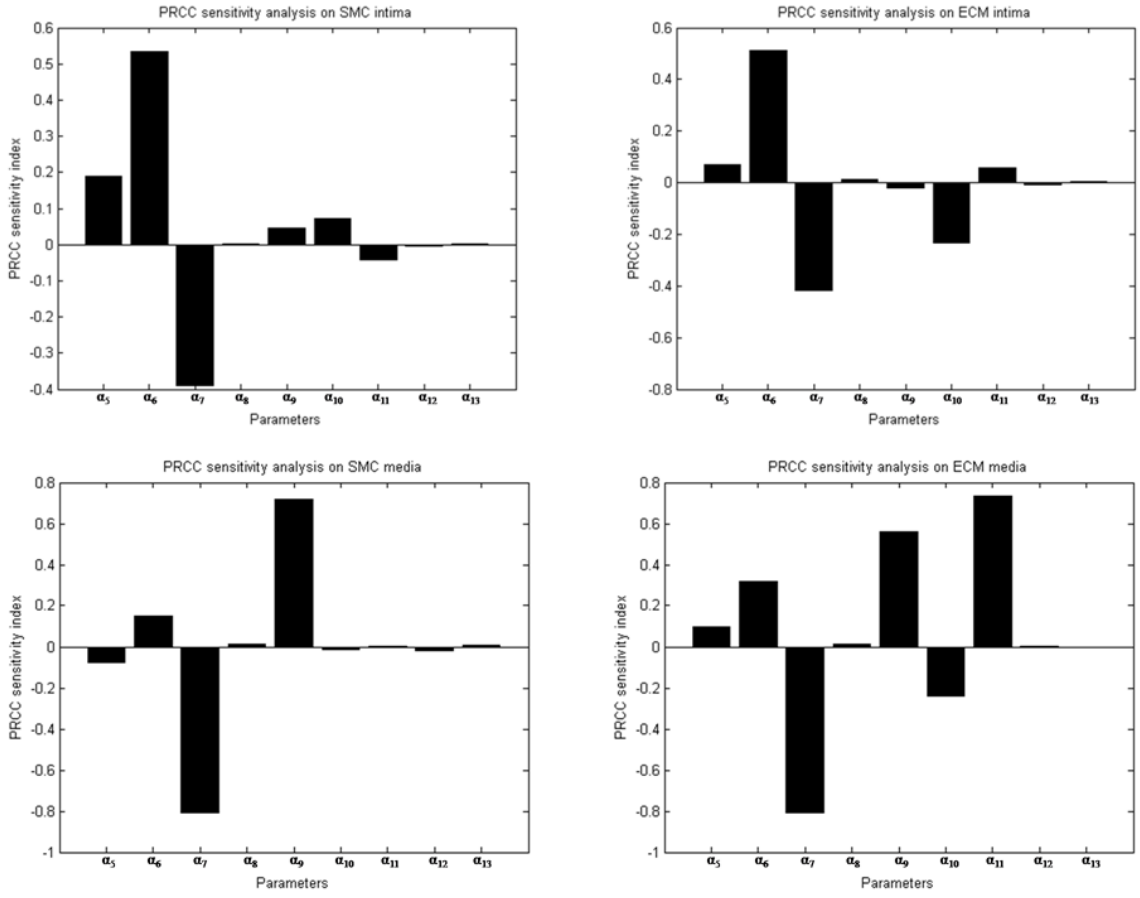

Figure 3.7: Nonlinear sensitivity analysis.

the vein graft adaptation; one is associated with the shear stress and another one with the transmural pressure (Figure 3.9). The relationship between various nodes in Figure 3.9 has been oriented with either positive or negative sign [2]. A positive sign between two nodes, A and B means that A is directly connected to the change of B. Whereas in case of a negative sign means that A is inversely connected to the change of B. We can clearly identify general types of recurrent feedback loops involving Shear-Lumen Area and Wall Tension-Wall Thickness from Figure 3.9. We can observe three closed cycles linking shear stress and lumen wall, one of them with

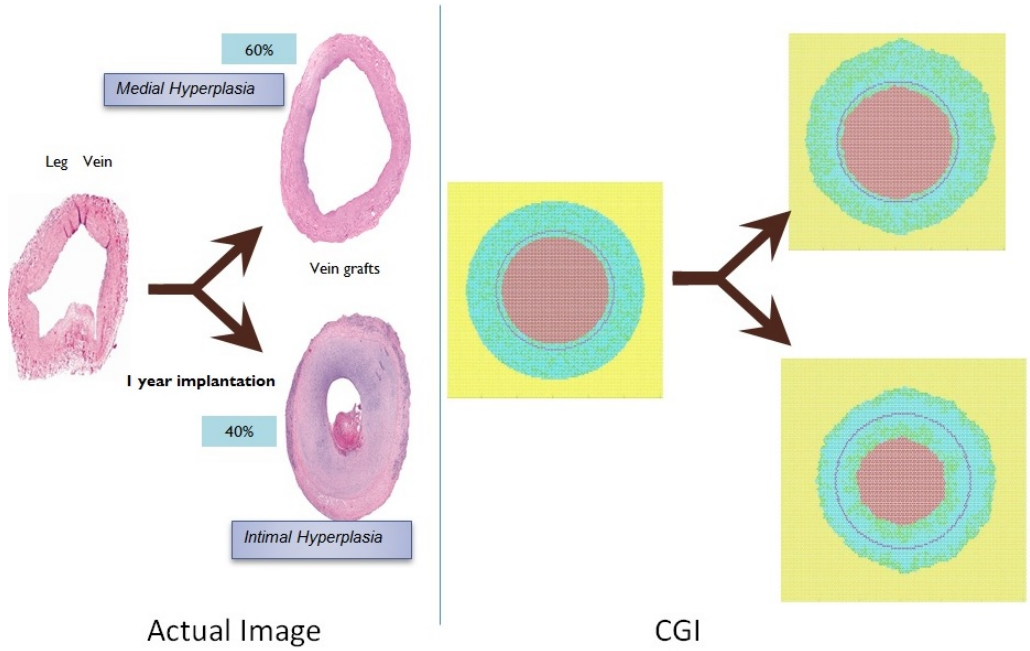

Figure 3.8: Pattern Formation (Actual image VS Computer generated image).

all positive signs (Shear $->$ Outward Remodeling $->$ Lumen Wall $->$ Shear) and two cycles with mixed signs along the path.

Similarly, we can identify two closed cycles linking 'Wall Tension' and 'Wall Thickness' (Figure 3.9), one of them with all positive signs. However, we can also find cross coupling relations between Shear - Wall Thickness, and Wall Tension - Lumen Area, respectively (Figure 3.9). This can lead to the fact of some of the interesting patterns formed (i.e., temporal oscillation between inward and outward remodeling) during vein graft adaptation. Now using this feedback mechanism along with the results of our sensitivity analysis, we would like to develop some sets of rules, which will help us to understand the formation of interesting pattern systematically.

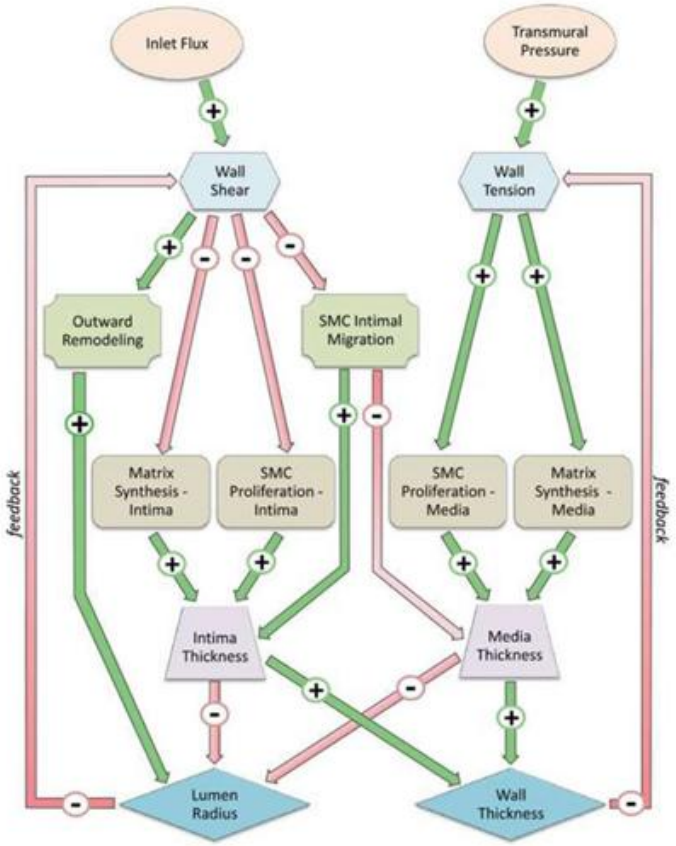

Figure 3.9: Feedback mechanisms in the vein graft adaptation [2].

3.3.1 Intimal Hyperplasia

Here we would like to develop some control mechanisms to explain the pattern formed during intimal hyperplasia. The feedback mechanism associated with the shear stress provides a control mechanism, where low shear stress increases the rate of SMC mitosis inside the intima and higher shear stress decreases this rate. We would like to apply this concept in our ABM-PDE model to explain the pattern formed here. At first, we would like to start from the basic solution. Let's consider the shear stress at this stage is τ_i , where our target shear stress is τ_t and $\tau_t > \tau_i$. Since low shear

stress promotes SMC division inside the intima, we will increase the probability of SMC division inside the intima applying the following rule:

$$P_{division} = \alpha_1(1 + \alpha_6 * (\tau_t - \tau_i)/\tau_t). \quad (32)$$

Our goal is to reach to the target high shear stress τ_t and hence, we increase the probability of SMC generation inside the intima by (32), which will increase intima thickening. Consequently, this intima thickening will reduce the radius of the lumen, which will ultimately increase the shear stress and reach to the target shear stress gradually. Once this target shear stress τ_t (i.e., $\tau_i = \tau_t$ in (32)) is achieved, the model will be again in the basic solution stage and stabilize gradually. In this way, we are trying to generate any interesting pattern associated with the intimal thickness, which will help to understand its formation ultimately.

In this particular testing, the ABM and the blood flow module have been updated while the transmural pressure is constant as the rule associated with the SMC division inside the intima is related with the shear stress only. Since the simulation algorithm is time dependent and the shear stress at each hour does not differ significantly and the stress calculation is also expensive with respect to time, so this module is updated after certain period (i.e., 5 days) to calculate the updated shear stress and transfer this stress value back to the ABM. This update procedure continues until the target shear stress is achieved.

We run the simulations for different values of intima proliferation rate (i.e., α_6 = 20%, 50%, 75%) and other parameter sets (α_1, α_2, α_3, α_4, α_5, α_6, α_7, α_8, α_9, α_{10}, α_{11}, α_{12}, α_{13}, α_{14}, α_{15}) with values (0.05, 0.008, 24*14, 24*60, 0, 0.75, 0, 20, 0, 0, 0, 0, 0, 0, 0) for 12 months. The value of β (1) is 2.25 and initial lumen radius is 30 (i.e.,

Number of cells). The initial shear stress is 0.08 (N/m^2) and the target shear stress is 0.12 (N/m^2). We run 15 simulations in 15 different processors and then take the mean of the results (i.e., number of SMC inside intima, lumen radius, shear stress, wall thickness) associated with this test. We plot the individual results along with the mean and standard deviation to understand the stochastic nature of our simulation. The following figures explain the simulation results of intimal hyperplasia. We apply the perturbation after 90 days to let the basic solution stabilize.

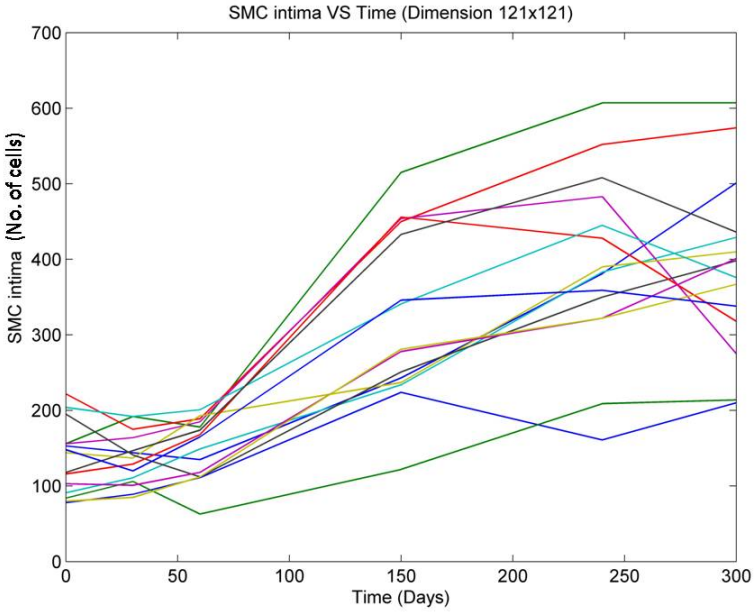

Figure 3.10: Logistic nature of SMC inside intima.

The result of intimal hyperplasia test shows logistic nature of the growth of SMC inside the intima (Figure 3.10) and shear stress (Figure 3.14), which leads to the fact that the model shows sensitivity as soon as we apply perturbation and becomes stabilized as soon as it reaches to the asymptote of the target high shear stress. The lumen area remains stable althrough this simulation (Figure 3.12).

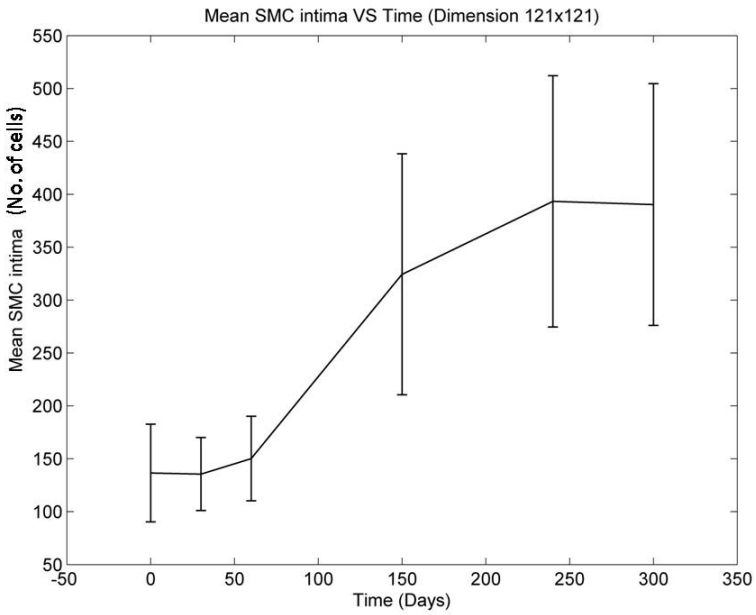

Figure 3.11: Logistic nature of mean SMC inside intima..

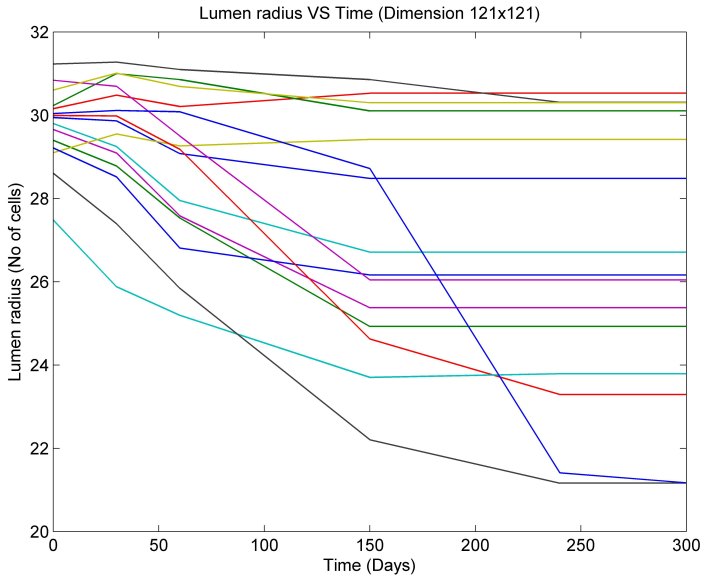

Figure 3.12: Stable nature of lumen radius.

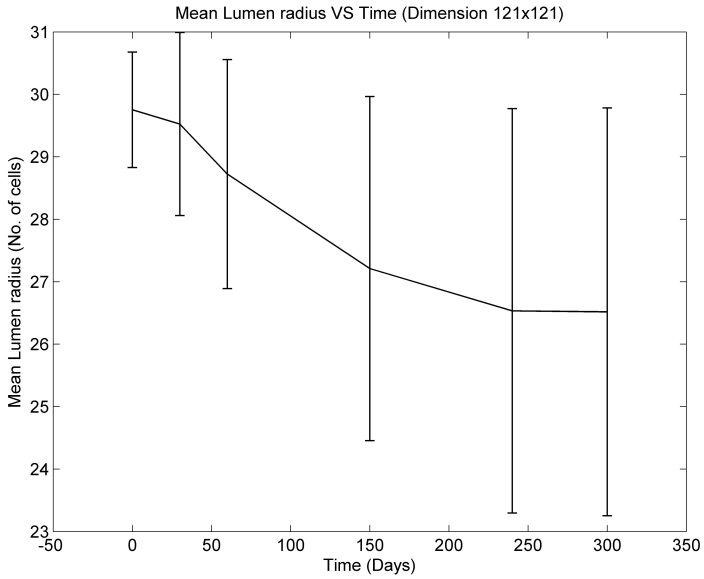

Figure 3.13: Stable nature of mean lumen radius.

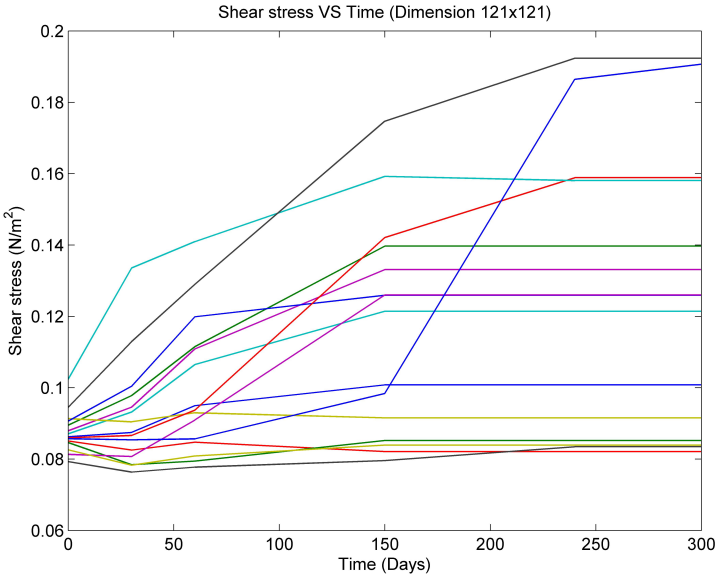

Figure 3.14: Logistic nature of shear stress.

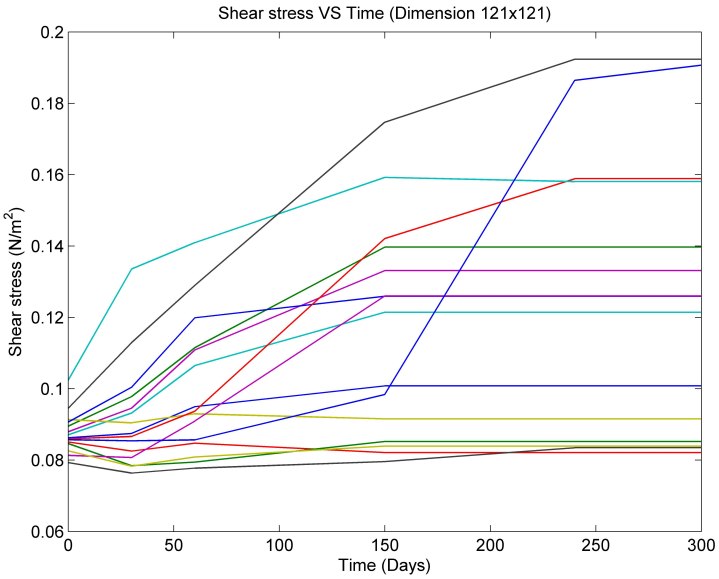

Figure 3.15: Logistic nature of mean shear stress.

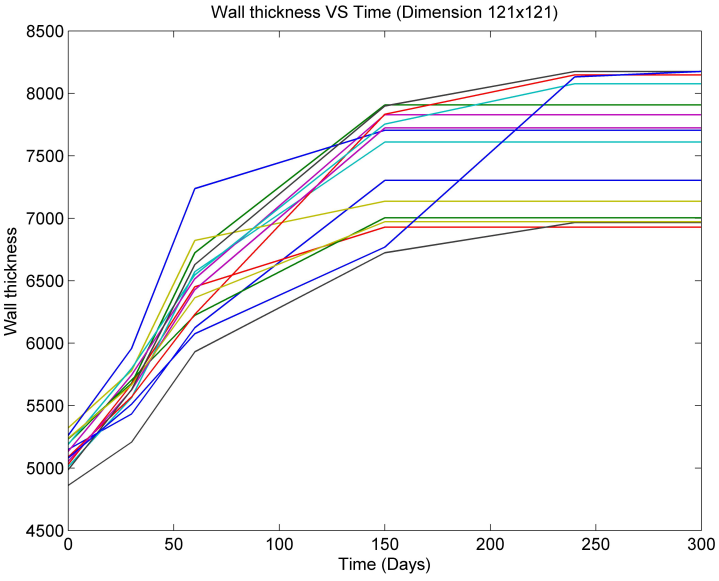

Figure 3.16: Growth of wall.

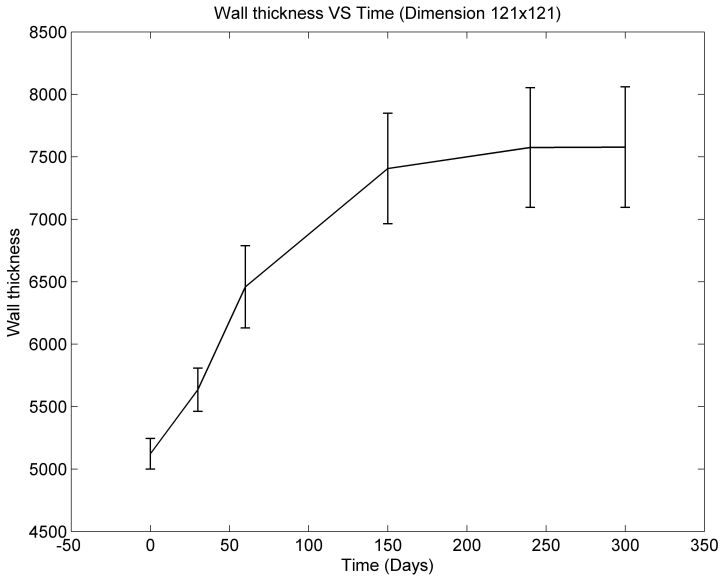

Figure 3.17: Growth of mean wall.

3.3.2 Medial Hyperplasia

There is another interesting pattern, which is of interest with the clinical observation of the vein graft adaptation, and it is known as the medial hyperplasia. This corresponds to the increase of SMC and ECM inside the media. There is one feedback mechanism associated with the tension (Figure 3.9), which is responsible for the medial growth [2]. From this feedback, it is observed that high tension promotes SMC division inside the media, which will increase the growth of media. This growth of media will reduce the tension generated by the surrounding wall of the vein graft, which will reduce the production of SMC/ECM inside the media.

So we would like to develop a control mechanism using the feedback mechanism associated with tension, which will help us to explain the pattern formed in medial hyperplasia. We will start from the basic solution this time as well. Let's consider

the tension at this stage is σ_i, where our target tension is σ_t and $\sigma_t < \sigma_i$. Initial high tension will promote SMC division inside the media following the rule:

$$P_{division} = \alpha_1(1 + \alpha_9 * (\sigma_i - \sigma_t)/\sigma_t). \quad (33)$$

Our goal is to reach to the target low tension σ_t, which will reduce the SMC/ECM generation inside the media. As a result, we increase SMC production inside the media by applying the probabilistic rule (33) and once the target tension is achieved (i.e., $\sigma_i = \sigma_t$), the model will be back in the basic solution stage and stabilize gradually. In this way, we are trying to form interesting pattern found in the medial hyperplasia so that this kind of pattern formation can be explained thoroughly.

In this particular test, the ABM and the tissue mechanic module have been updated with respect to time as the rule associated with SMC division inside the media is related with tension only (33). So the tissue mechanic module is updated after certain period (i.e., 10 days) to calculate the tension, as the update of the tissue mechanic module at each hour is expensive and the tension does not change within this short period of time significantly. This update of tissue mechanic module is continued until the target tension is achieved.

We run the model with the parameter set (α_1, α_2, α_3, α_4, α_5, α_6, α_7, α_8, α_9, α_{10}, α_{11}, α_{12}, α_{13}, α_{14}, α_{15}) and their values (0.05, 0.008, 24*14, 24*60, 0, 0, 0, 20, 0.20, 0, 0, 0, 0, 0, 0) respectively for 12 months. The value of β (1) is 2.25 and initial lumen radius is 30 (i.e., number of cells). The initial tension is 0.43 N and the target tension is 0.38 N. We run 15 simulations in 15 different processors and then take the mean of the results (i.e., number of SMC inside media, tension, wall thickness etc.).

The following figures explain the simulation results of medial hyperplasia. We apply the perturbation after 90 days to let the basic solution stabilize.

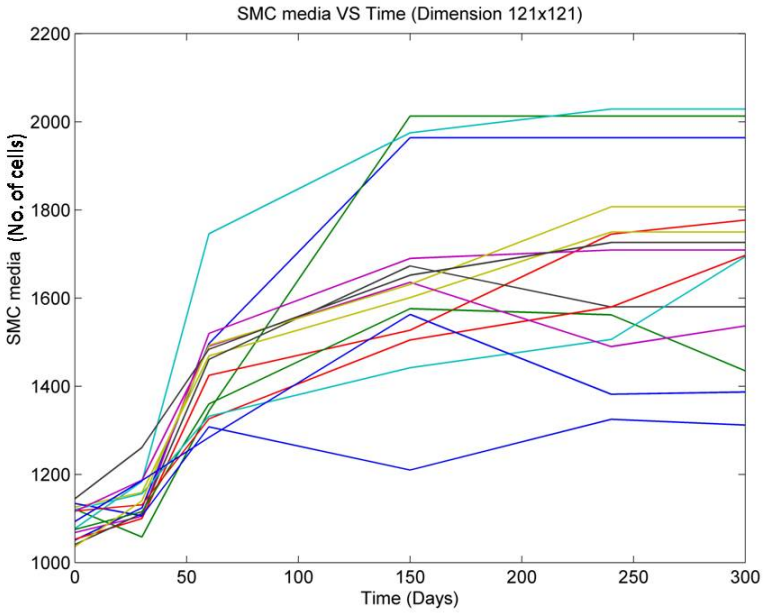

Figure 3.18: Logistic nature of SMC inside media.

The result of medial hyperplasia test shows that the growth curve of SMC inside the media has logistic nature. Another interesting feature of this test is that lumen radius does not change significantly (Figure 3.23), which is relevant with actual clinical observation.

3.3.3 Temporal Oscillation

In this section, we show the competition between the intimal hyperplasia and outward remodeling. In this case, section 3.3.1 and section 3.3.2 have been combined with different perturbation rate (i.e., 50%, 10%) of the parameters (α_6, α_9) of interest.

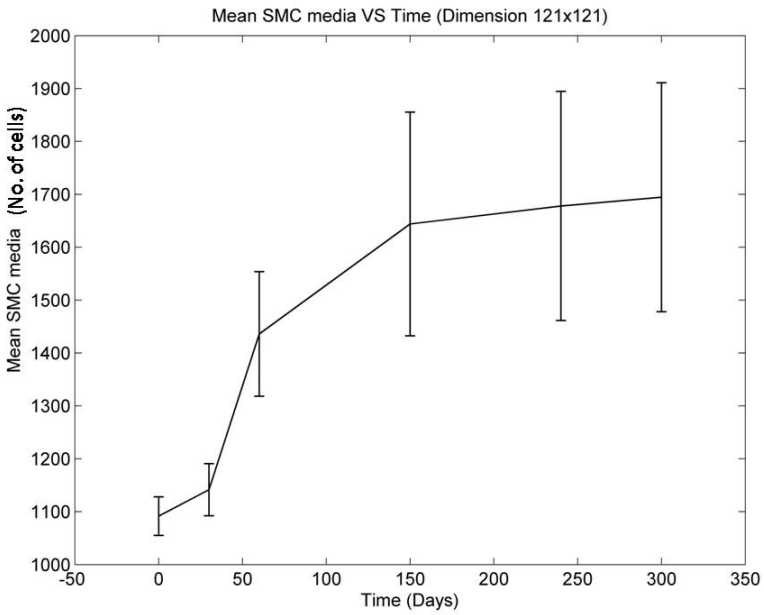

Figure 3.19: Logistic nature of mean SMC inside media.

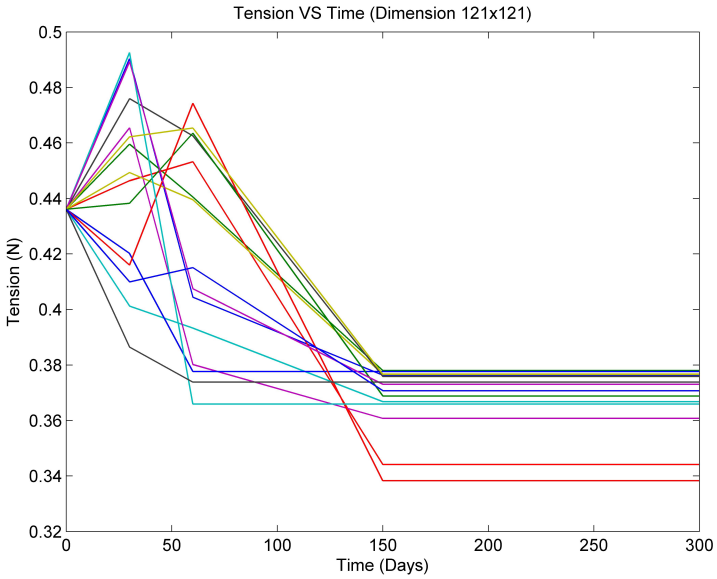

Figure 3.20: Decrease of tension.

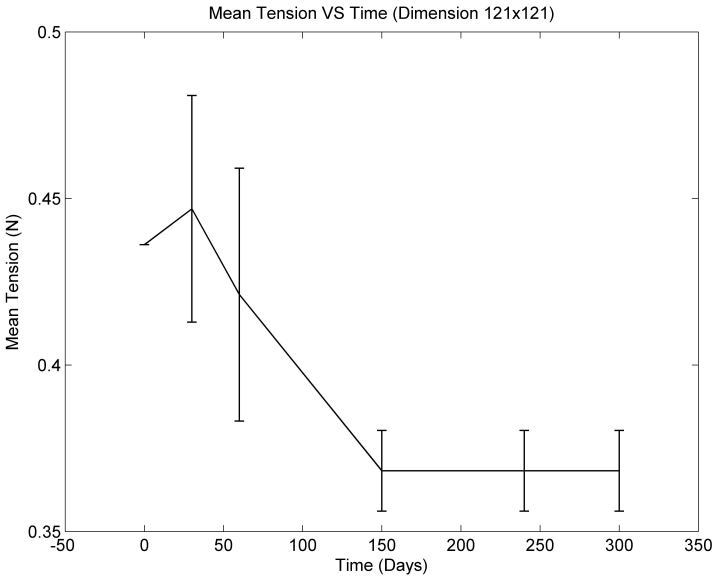

Figure 3.21: Decrease of mean tension.

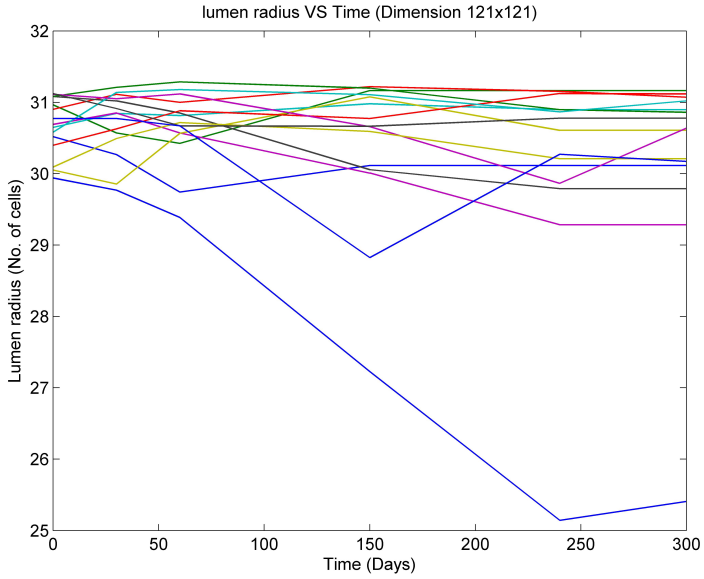

Figure 3.22: Stable nature of lumen radius.

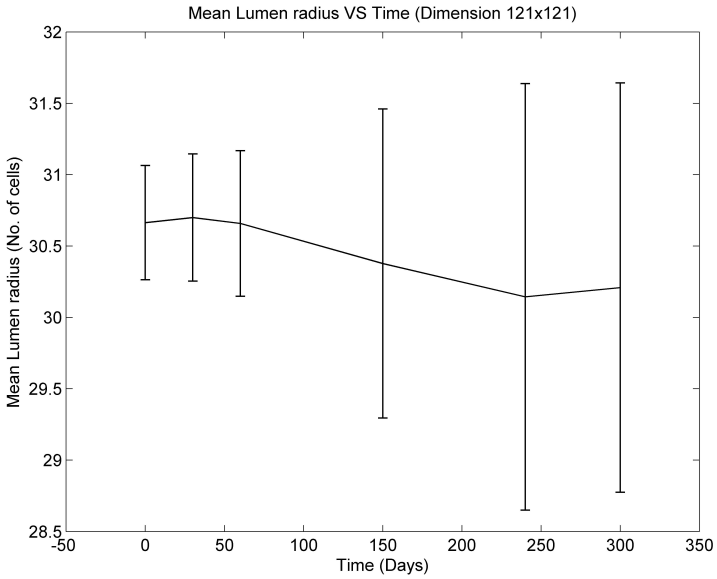

Figure 3.23: Stable nature of mean lumen radius.

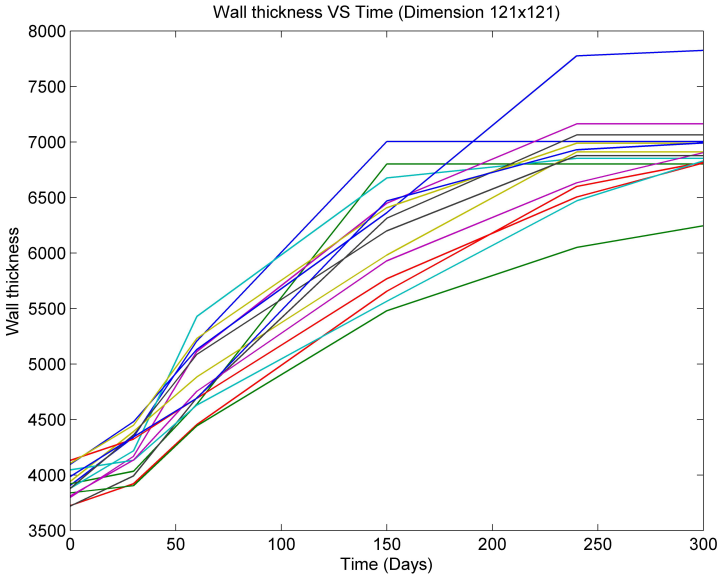

Figure 3.24: Growth of wall thickness.

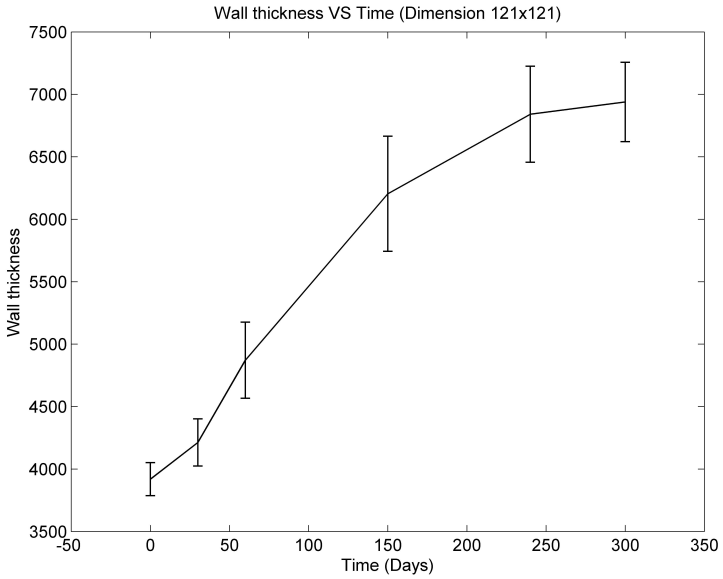

Figure 3.25: Growth of mean wall thickness.

Another important feature of this testing is that we apply high perturbation rate (100%) of ECM degeneration ((19) and (21)) to have oscillatory patterns. It is because of the fact that both the previous testings increase the number of SMC inside the intima and media. As a result, we have applied perturbation in the ECM degeneration by an SMC to get oscillatory patterns of the lumen and the wall. We run 10 simulations in 10 different processors and plot the variation of lumen radius and wall thickness individually with the total variation as well. The total variation has the following formula:

$$TotalVariation = \sum_{i=1}^{n}(|V_{ti} - V_{t(i-1)}|)/n, \quad (34)$$

where V_{ti} is the lumen radius or wall thickness at time step t and n is the number of processors.

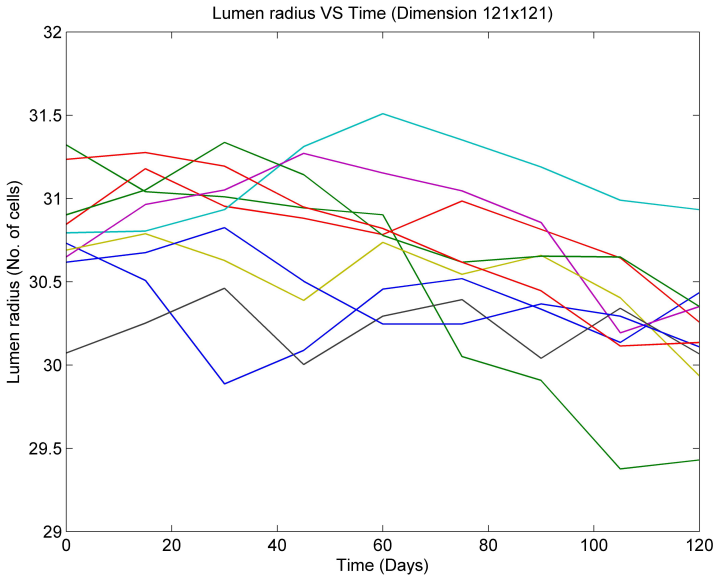

Figure 3.26: Oscillatory characteristic of the lumen radius.

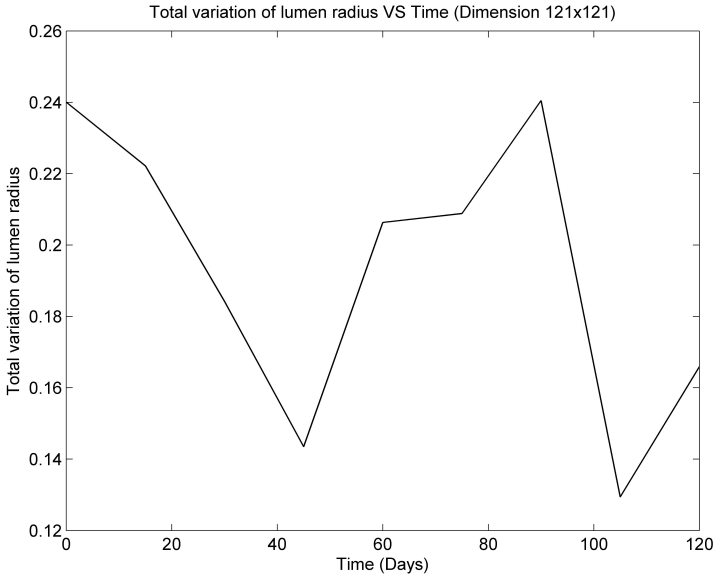

Figure 3.27: Oscillatory characteristic of the total variation of the lumen radius.

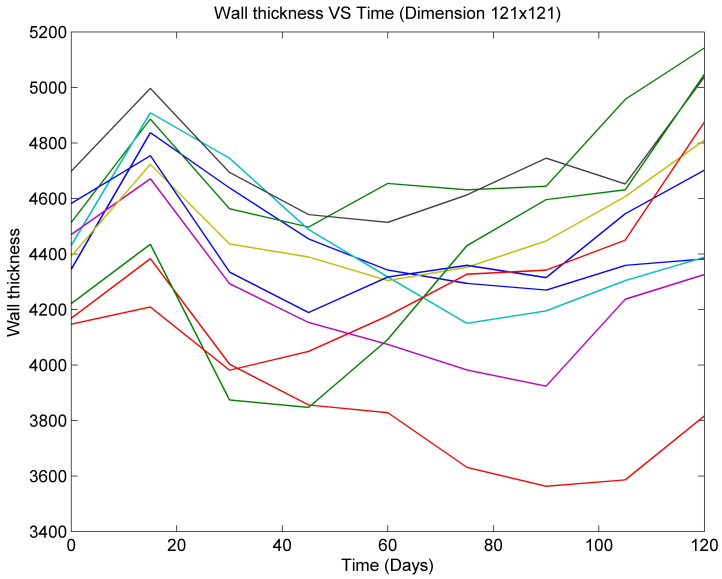

Figure 3.28: Oscillatory characteristic of wall thickness.

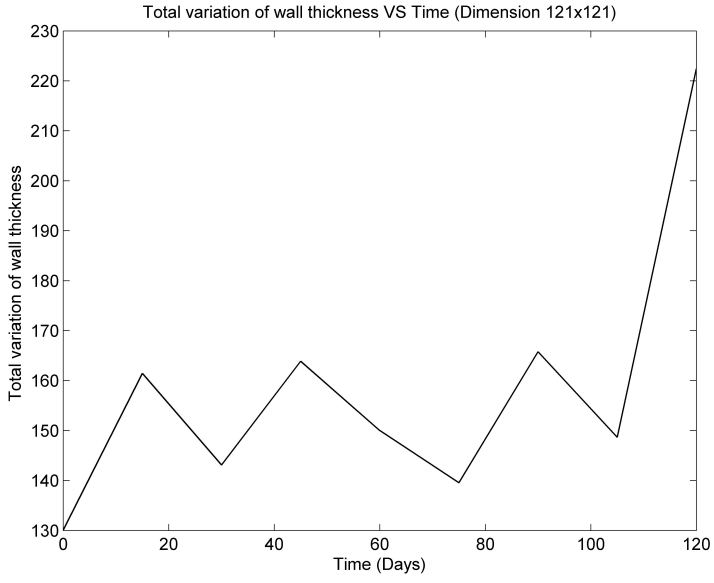

Figure 3.29: Oscillatory characteristic of the total variation of wall thickness.

The interesting feature of this temporary oscillation is that both the variation of the lumen radius and wall thickness show periodic change in the course of time, which is relevant to the clinical observations [59].

3.3.4 The validation of different kinds of patterns generated by the model

We have explained a number of specific pattern formations in the previous sections. In this section, we would like to focus on different pattern formations associated with different shear stresses and a fixed tension and how we can explain this pattern formation with the framework. This analysis will help to advance the validation of our model with real histological data sets.

Nonlinear histological data fitting is a very difficult task. We are interested to explain such patterns. Before explaining such real histological patterns, we would like to fit virtual (i.e., simulated) set of experimental data (i.e., histological data sets of rabbits vein grafts [1]) by the model. As a result, we would like to define an efficient objective function with which the fitting is accomplished at first. Next, we would like to couple a genetic algorithm (GA) having that efficient objective function with the model to validate the fact that the simulated data sets are reproducible in a multivariate data analysis environment. As a result, this analysis will reduce the gap in understanding the formation of nonlinear histological data sets.

The definition of the objective function comes from the key parameters of the model. We have introduced an efficient approach to determine the required objective

function to fit nonlinear simulated histological data sets. The simulated data set corresponds to the area of the lumen and the density map of SMC in the intima and media. We have considered these two types of data sets, since these are easily available from biological experiments [1]. The density map of SMC means the ratio of a cell′s distance from the lumen (d) to the thickness of the wall ($d^{/}$) (Figure 3.30).

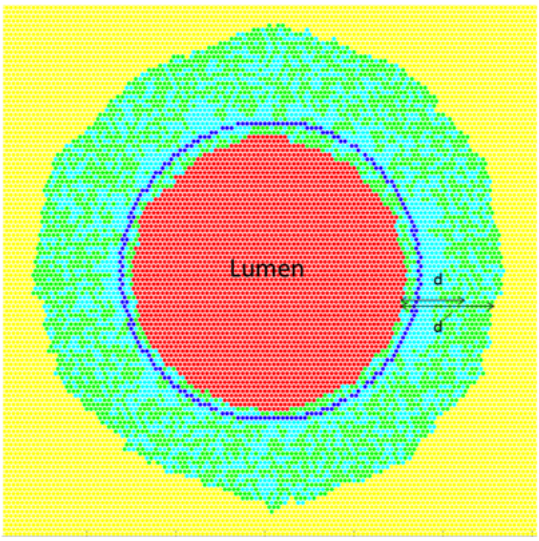

Figure 3.30: The calculation of SMC density map. The ratio of $d/d^{/}$ represents the density map of SMC outside the lumen.

As a result, this SMC density map divides the entire wall into different regions based on the ratio (i.e., 0.1 to 1.0). The density of SMC will differ based on different shear stresses and tension and the perturbations of the parameters. We have generated the simulated data sets while varying the shear stress (i.e., low, average and high stress) and three key parameters (i.e., α_5, α_6, α_9) and other three parameters (i.e., α_{12}, α_{13}, α_{15}). Additionally, we have applied 0.6N of transmural pressure. As a result, the simulated data set corresponds to high (5 times higher than the average

stress), low (10 times lower than the average stress) and average shear stress (10 times higher than initial stress) with different perturbation (i.e., 10%, 50%, 40%, 30%, 10%, 20%) of the parameters (i.e., α_5, α_6, α_9, α_{12}, α_{13}, α_{15}) respectively. The rest of the parameters have the values of the basic solution of the model.

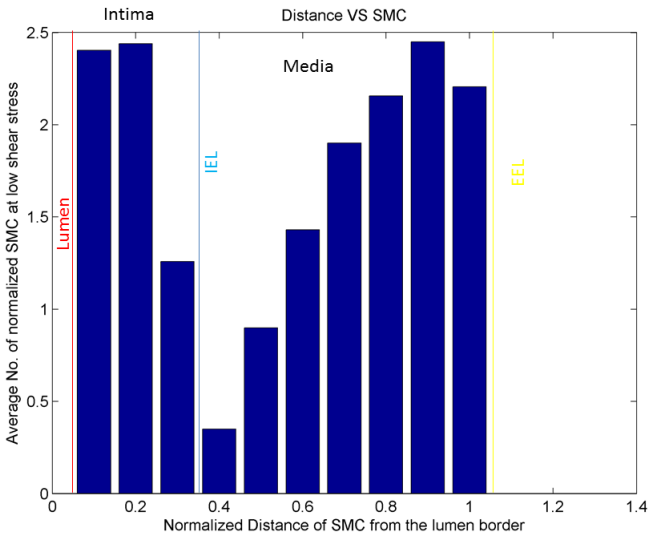

Figure 3.31: SMC density map at low shear stress.

We have generated 15 sets of virtual data sets (i.e., lumen area, SMC density map) with the aforementioned settings of the parameters for a month long of simulation. This 15 data set is divided into three groups based on the shear stress (i.e., low, average, high), where each group has five data. The density map of SMC has been normalized with the initial density map of SMC to understand the proliferation of SMC in different regions of the vein graft (i.e., Figure 3.31 to Figure 3.33). The average area of the lumen at different shear stress has been also considered to define the objective function.

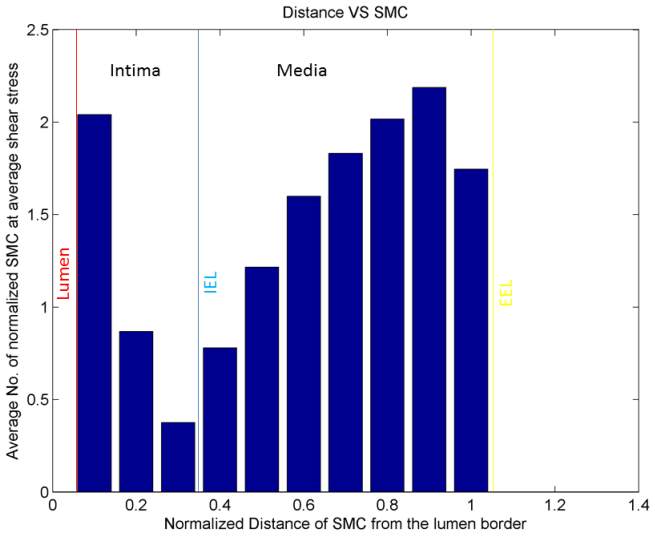

Figure 3.32: SMC density map at average shear stress.

The objective function will help to regenerate the simulated data sets. We will run the simulation with different perturbation of the parameters while keeping the range of the shear stress and tension similar to the already generated histological data sets. This will allow the objective function to compare the new data sets with the simulated data sets and the objective function with the best local minimum will be the required objective function. It is expected that the objective function will generate the local minimum at the simulated distribution of the parameters. As a result, we will be able to retrieve the simulated distribution of the parameters from the objective function. This analysis verifies the fact that the model can regenerate the simulated data sets, which can be ultimately applied in matching real histological data sets as we will follow up in the next.

We are interested to retrieve the distribution of one single key parameter at first.

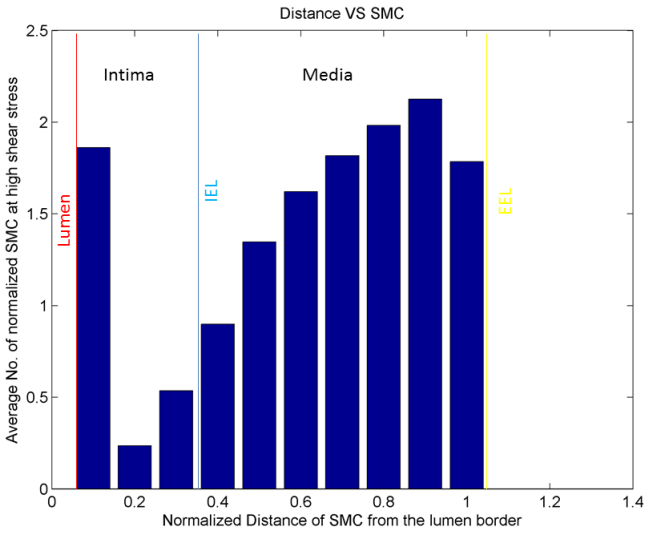

Figure 3.33: SMC density map at high shear stress.

Next, we will advance our analysis to retrieve the distributions of two key parameters. Finally, we will highlight on the retrieval of more than two key parameters. There will be a number of objective functions and we will pick the best-fit one based on the simulation results. The objective functions associated with a key parameter are as follows:

$$F1_{objective}(\alpha_i) = \sqrt{\sum_{j=1}^{3}(\|A_j^G - A_j^S\|/A_j^S)^2}, i\epsilon\{5,6,9\}, \quad (35)$$

$$F2_{objective}(\alpha_i) = \sqrt{\sum_{j=1}^{3}\sum_{k=1}^{10}(\|D_{jk}^G - D_{jk}^S\|/D_{jk}^S)^2}, i\epsilon\{5,6,9\}, \quad (36)$$

$$F3_{objective}(\alpha_i) = w_1 * F1_{objective}(\alpha_i) + w_2 * F2_{objective}(\alpha_i), i\epsilon\{5,6,9\}. \quad (37)$$

Here A_j^S and D_{jk}^S are the simulated data sets, which correspond to the average area of the lumen and the SMC density map respectively. Next, we would like to regenerate the simulated data sets. As a result, we will run the simultion program with a deviation (i.e., low to high) of the distribution of the key parameters from

the simulated distribution. This generated data sets correspond to A_j^G and D_{jk}^G respectively in the above equations. This provides a detail analysis on the distribution of the key parameter against the objective function as it is shown in the following figures (i.e., Figure 3.34 to Figure 3.36).

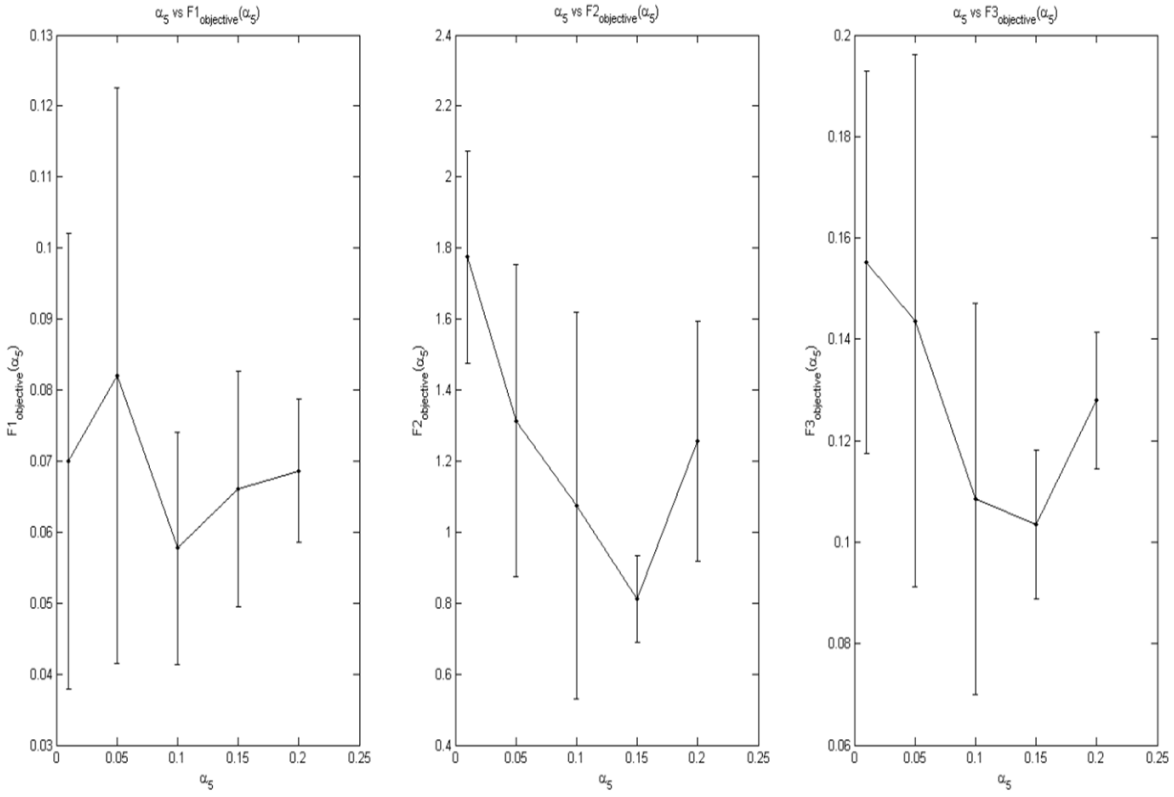

Figure 3.34: α_5 VS objective functions.

It is evident from Figure 3.34 to Figure 3.36 that the three key parameters (i.e., α_5, α_6, α_9) regenerate the simulated data sets at their corresponding simulated distribution (i.e., 10%, 50%, 40%) respectively. As a result, we get the local minimum of the objective functions at the simulated distribution of the key parameter. We have added $w_1 = 0.95$ and $w_2 = 0.05$ in equation (35) to get the local minimum

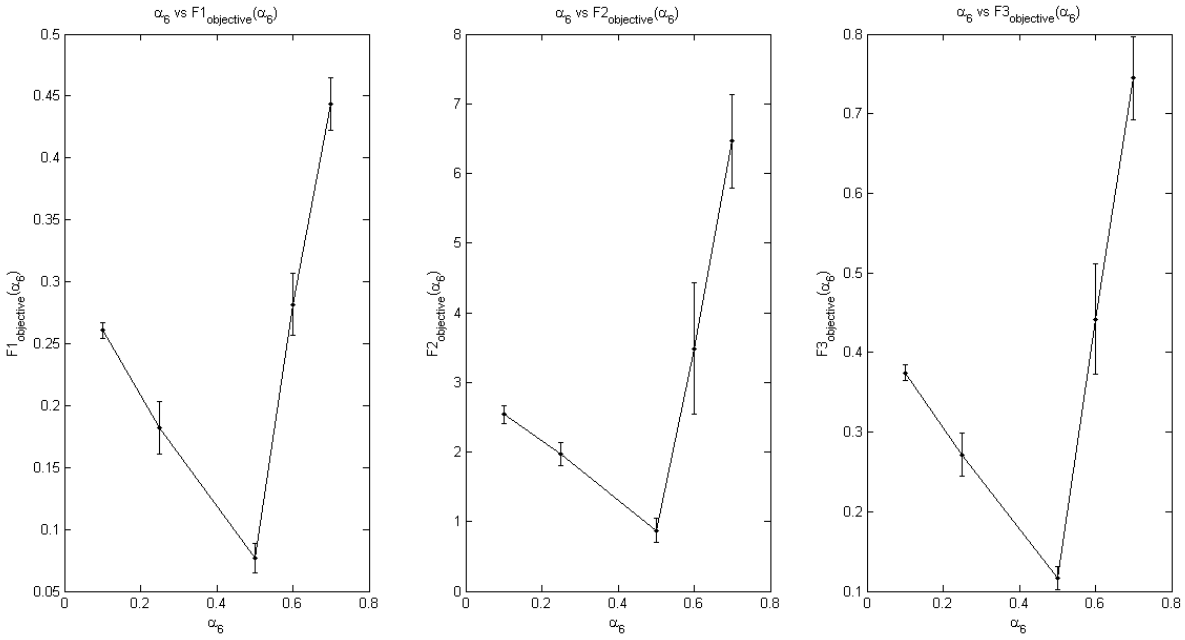

Figure 3.35: α_6 VS objective functions.

of the objective function at the simulated distribution of the key parameters. This represents the best fit objective function.

One interesting observation from this single key parameter retrieval test is that parameter α_5 shows slight deviation from its corresponding simulated distribution in (36). We get the local minimum of equation (36) of α_5 at 0.15%, whereas the simulated value of α_5 is 10%. It is because of the fact it is not directly involved in SMC/ECM division/apoptosis. However, we get the best result for α_6 since it is directly involved in the division/apoptosis of SMC/ECM. The parameter α_9 also shows expected result for all the objective functions. This is how we can retrieve the distribution of the key parameter from the simulated data sets.

Next, we would like to advance our analysis to regenerate the simulated data

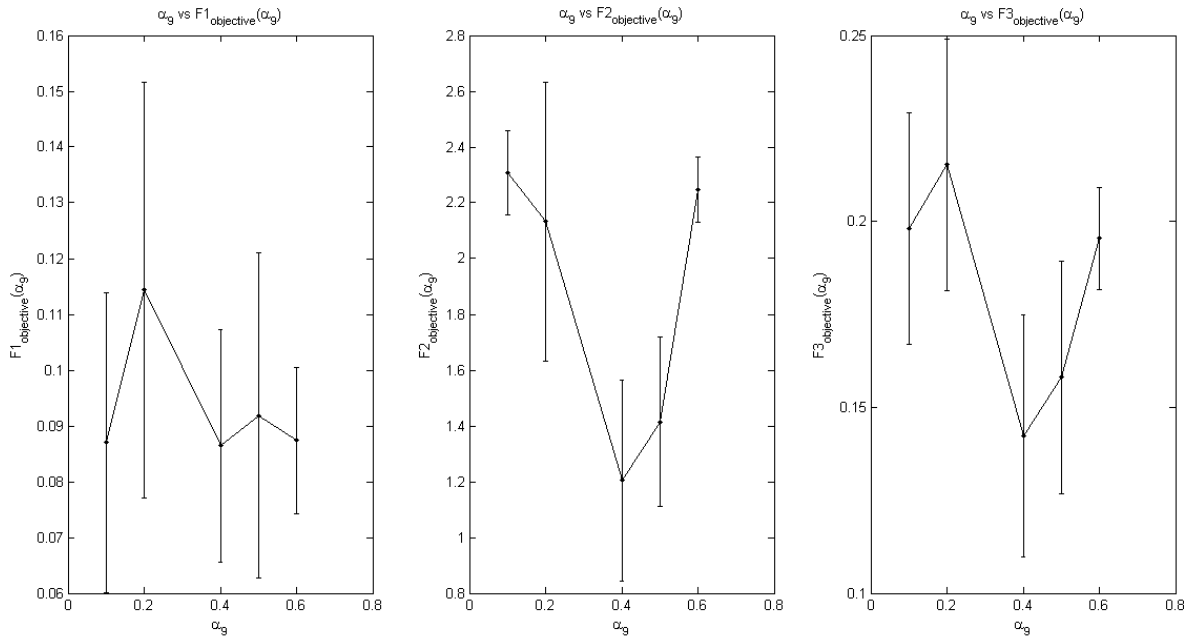

Figure 3.36: α_9 VS objective functions.

sets with two key parameters. This requires running the simulation program, while sampling the two key parameters within the simulated distribution. Next, we can calculate and plot equations (35) to (37) for different values of the key parameters. This will provide a two dimensional solution space of the objective functions. We can retrieve the distribution of the key parameters from the local minimum of this solution space. We have observed from Figure 3.37 to Figure 3.39 that the local minimum of the objective functions corresponds to the simulated distribution of the key parameters. This also proves the fact of regenerating the simulated data sets with two key parameters.

It is evident from Figure 3.37 to Figure 3.39 that the two key parameters regenerate the simulated patterns (i.e., dark blue-colored surfaces in Figure 3.37 to

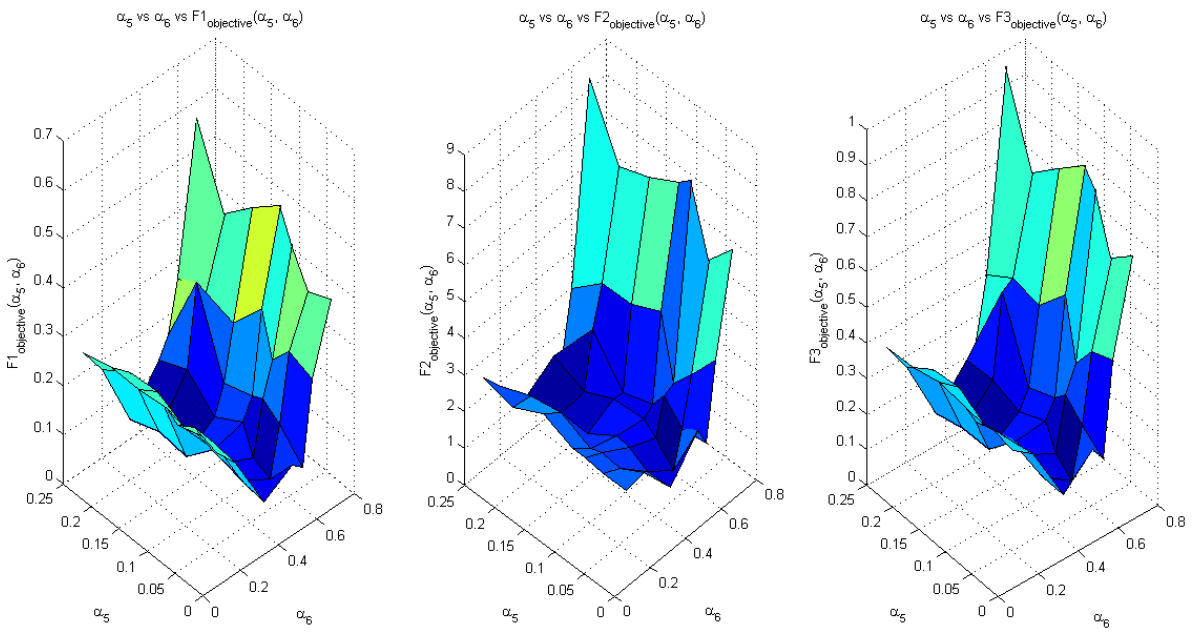

Figure 3.37: α_5 VS α_6 VS objective functions.

Figure 3.39) at the corresponding simulated distributions. We have also done surface response by a key parameter in the two dimensional solution spaces of the objective functions. This represents the characteristic of the local minimum of the objective functions. It is evident from Figure 3.40 to Figure 3.42 that the surface response by a key parameter is consistent with the local minimum of the objective functions. As for example, α_6 represents the local minimum at its simulated distribution (i.e., 50%) in figure Figure 3.40. It is also consistent with other two key parameters. The surface response generated by the key parameters also provides a 'concave' shape solution space, where the local minimum is the deepest surface of the cave.

Finally, we would like to advance our analysis of regenerating the simulated patterns with more than two key parameters. This will increase the solution space (i.e.,

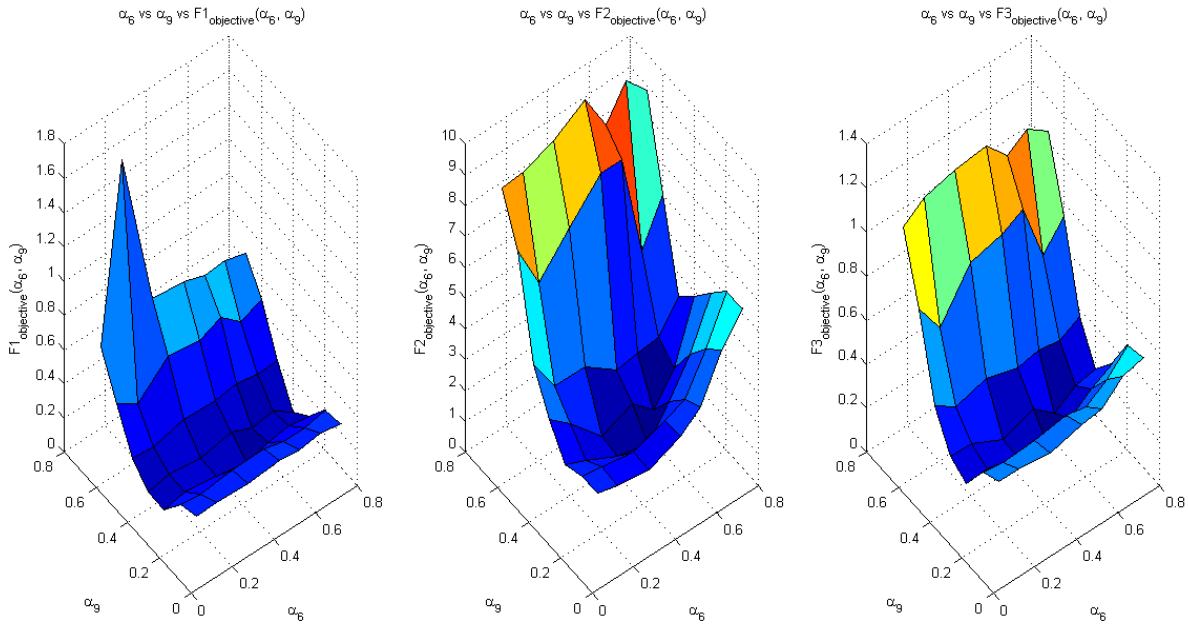

Figure 3.38: α_6 VS α_9 VS objective functions.

at least 10^3). As a result, we would like to couple a genetic algorithm (GA) with the model to retrieve the distribution of the key parameters from the simulated data sets. This coupling will help to find the best-fit solution, since the GA can play the most significant role browsing through the best-fit parameter sets [60], whereas the model is responsible for the calculation of the objective function. As a result, we can calculate the objective function for a specific set of parameters, which corresponds to a population of the GA. This coupling can become very efficient with respect to nonlinear data fitting as we will explain in the following.

We have used a traditional GA (i.e., Figure 3.43) having all the characteristics (i.e., crossover, mutation etc.) of a GA. Initially, the GA generates a number of

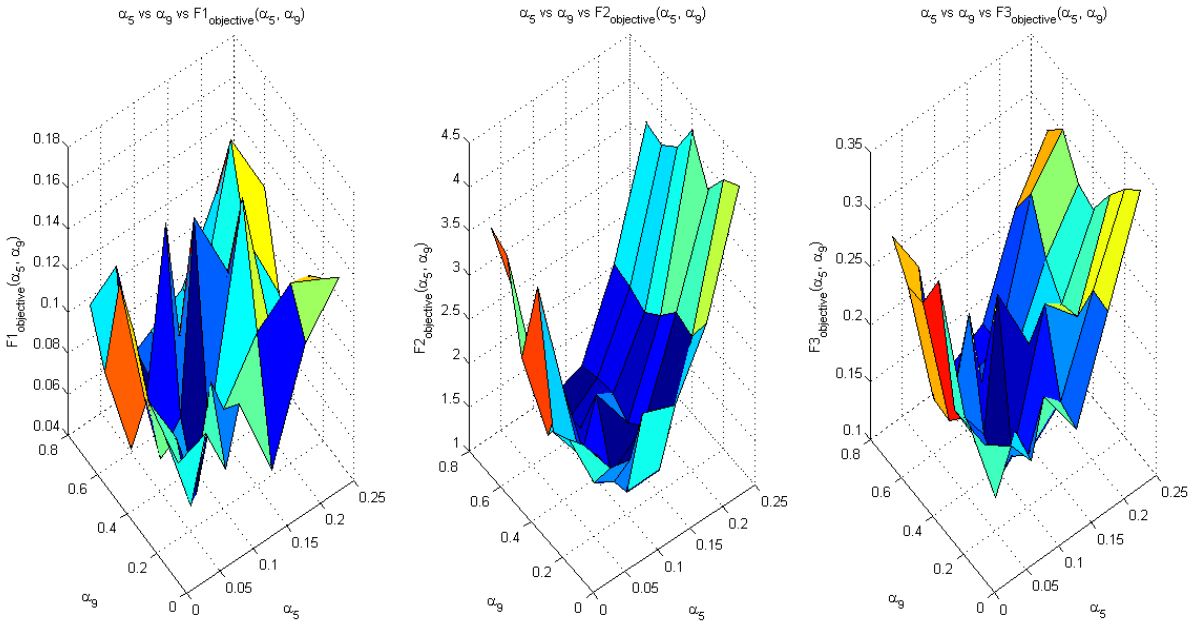

Figure 3.39: α_5 VS α_9 VS objective functions.

populations each of which consists of a number of gene. Actually, these genes correspond to the key parameters (i.e., α_5, α_6, α_9). As a result, each population has three genes located in three consecutive positions. The model receives the population sets from the GA and then returns the value of the objective function associated with the population (i.e., Figure 3.44). Here, the objective function is the fitness function of the population. Next, the GA continues with the crossover and mutation based on the fitness function of the population and sends a new set of population to the model. This continues until the GA finds the best-fit population (i.e., Figure 3.43).

All the genes we have used have real values ref [61, 62]. This provides more variation in the populations [63] and there is no conversion needed for a real number to a binary form for the GA. The GA follows certain steps to perform crossover

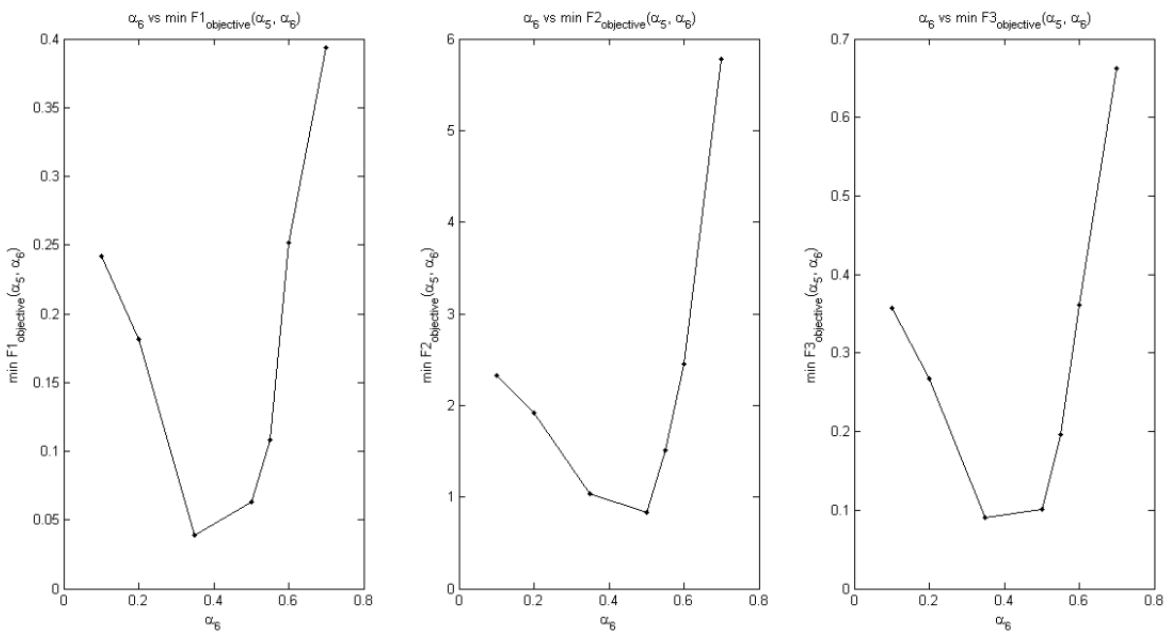

Figure 3.40: Surface response by α_6 from Figure 3.37.

and mutation over the existing population. It selects two populations to perform crossover and mutation. The probability of selecting a population is proportional to its fitness. In crossover, the GA distributes the genetic values of two selected parents over the populations. This distribution occurs at a particular index position (i.e., crossover index) selected between the size of each population randomly. However, crossover does not guarantee information that is nonexistent with the population. The mutation is responsible for this property, while injecting new genetic values in the population. In mutation, the GA generates a random number between 0 and 1/mutation_rate (i.e., muatation_rate=0.10) for each of the gene in a population. If it is 0, then the corresponding gene is sampled between [0,1]. Otherwise, the genetic values are received from two selected parents. The GA copies the genetic values from the first parent if gene position $<$ crossover index; otherwise from the second parent.

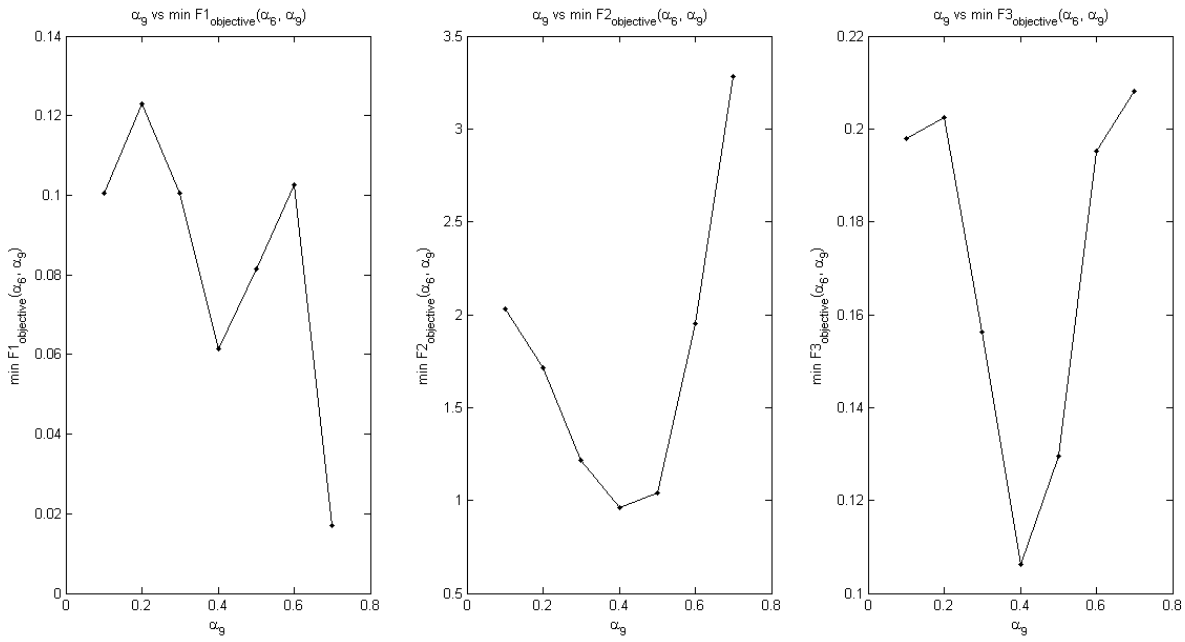

Figure 3.41: Surface response by α_9 from Figure 3.38.

The above properties of the GA ensure that the local minimum of the objective function can be achieved after a number of generations. However, the number of generations can be large to find out the local minimum. This depends on the population size as well. Generally, more population will provide more variation to the solution, which will ultimately help the GA to reach to the local minimum. However, the size of the population also depends on the computing resource of the system. Based on the available computing resource, we have been able to use 100 populations to run the GA.

The GA initializes these 100 populations with uniform random distribution and sends to the model. We have considered the third objective function (37) for the GA to minimize, since this function combines other two objective functions as well. Next,

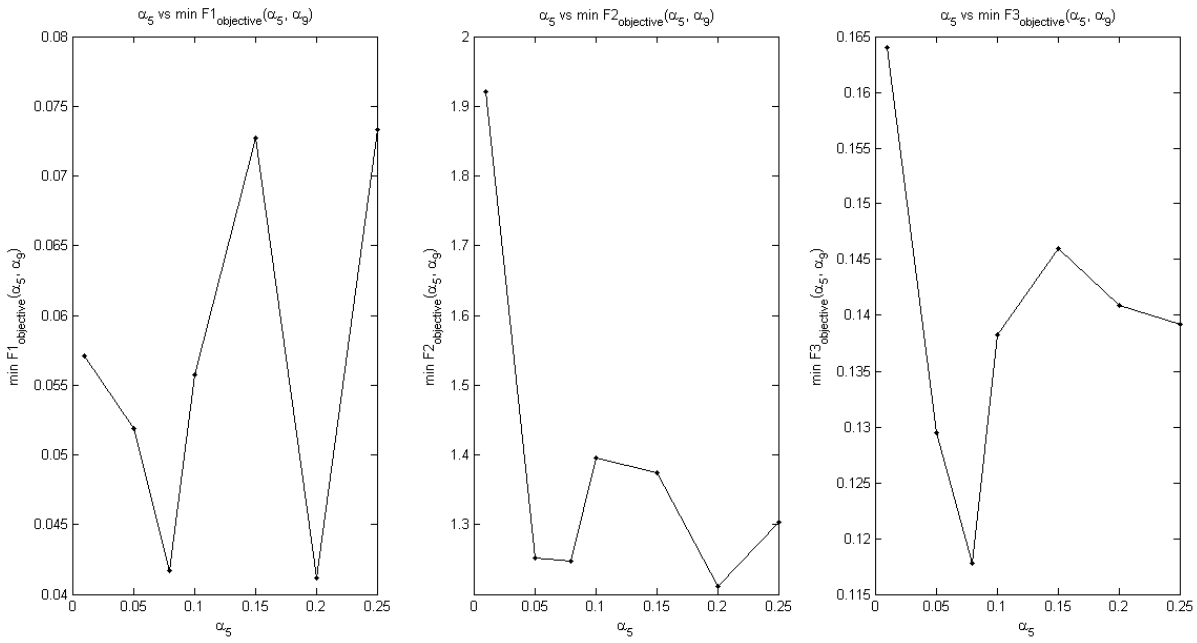

Figure 3.42: Surface response by α_5 from Figure 3.39.

we have run the GA for a number of generations and kept track of the minimum objective value at each generation (Figure 3.45) to figure out the convergence of the GA.

We have observed interesting result from the GA. The GA retrieves the local minimum of (37) at different generations (i.e., first, third etc)(Figure 3.41). This is an interesting feature of the GA, where sampling the best-fit populations might shift the local minimum. As a result, the local minimum shifts upward and then again moves downward after a number of generations. It is because of the fact that the GA performs the crossover and mutation among the existing populations to generate new populations. Above all, the model has high standard deviation. As a result, we have retrieved the distribution of the key parameters at different generations of the

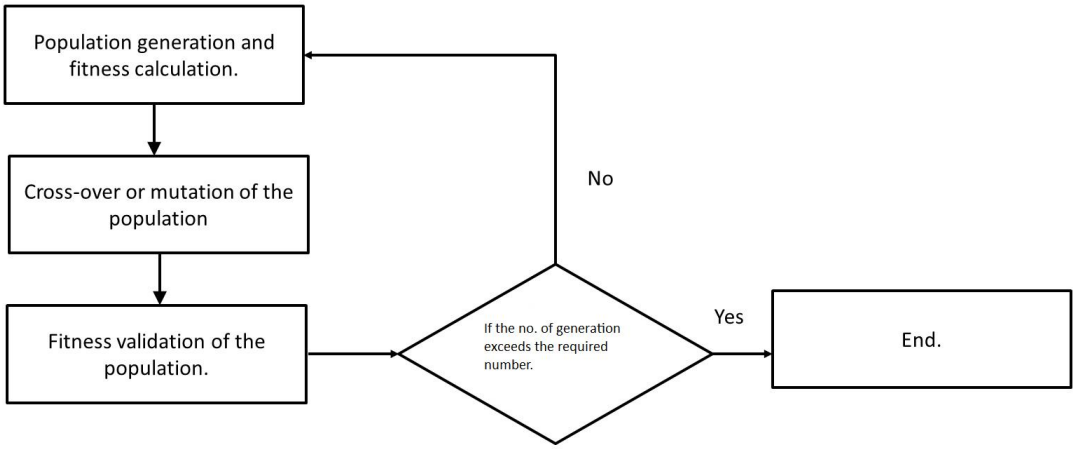

Figure 3.43: The genetic algorithm (GA).

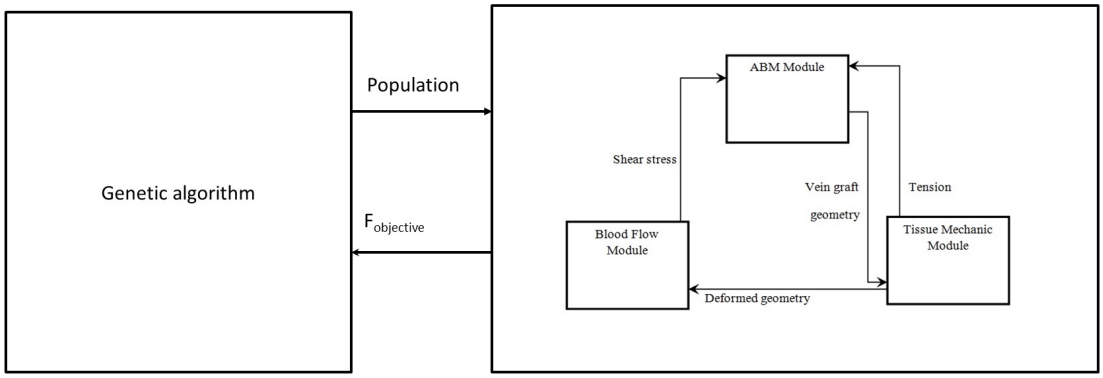

Figure 3.44: The coupling of GA with the model.

GA, since it is same as it is in the single and double parameter retrieval tests, while in other generations the local minimum shifts. This proves the fact that the model can regenerate the simulated patterns with three key parameters. We can apply this novel approach, while fitting real histological data sets [64].

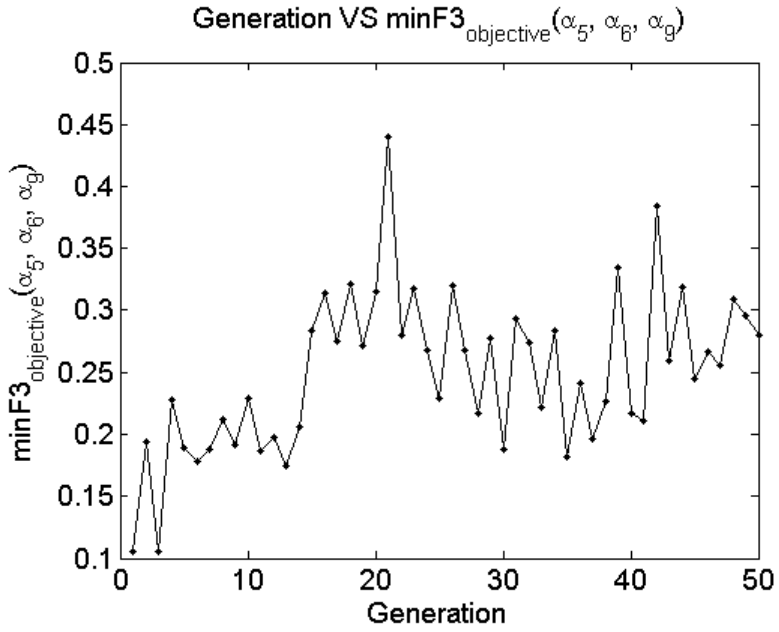

Figure 3.45: Generations VS $minF3_{objective}$.

Chapter 4

High-Performance Computing

In this section, we would like to focus on the implementation details of our computational framework. Our framework is modular consisting of different modules responsible for different actions followed by the data flow among the modules. Our implementation focuses on easy to understand development, where we keep the scope of agile development in our framework to test and validate different hypothesis associated with the vein graft adaptation. Our goal of developing the framework remains in the fact of identifying key parameters responsible in the vein graft adaptation and then regenerating specific patterns of the vein graft with those parameter sets. The selection of the key parameters of the model requires the execution of the model with different range of values of the parameters. As a result, we have incorporated parallel architecture into our framework to run and test our model with different sets of values of the parameters efficiently.

4.1 Module Development

When we start the implementation of the model from the scratch, we use a Matlab code that allows fast prototyping and presents an easy visual understanding of the ABM. The implementation is easy to debug but very slow in respect of computation time. Matlab or other related software allows easy to visualize implementation of the model. Here the surgeons can be in the design loop as well to get the feedback for correct implementation.

Once this agile development is finished and we are confident about this Matlab version of our model, we port this version to C. This C version is fast, modular and easy to understand. The similarity of naming functions and variables in these two versions also helps to keep track between this two versions. Finally, both the versions have been tested with same sets of random numbers to verify the fact that both the versions generate same output.

Modules	Execution time (s)
ABM	1406
Tissue Mechanic Module	726
Flow Module	14
Data transfer between modules	3

Table 4.1: Execution Time of different modules (Simulation time: 1 month, dimension of the grid: 121x121).

An example of execution time of our model executed on a single processor, is shown in Table 1. The total execution time is more than 12 times faster than the Matlab version. We have undertaken the following steps to speed up the C version:

• The memory allocation and deallocation is an expensive operation in computer programming. As a result, we have used static memory space in the heap, since the heap memory space is fast enough to access [65]. This speeds up our C version since it does not require memory allocation or deallocation at each simulation hour.

• The simulation program scans through each cell site in a random order at each simulation hour. As a result, we have used bijective mapping [66] between the cell index and a random number associated with that index. Next, we sort the random numbers in nondecreasing order and finally, the program accesses the cell index based on the sorted random numbers. We have applied merge-sort to sort the random numbers, since this is one of the fastest sorting algorithms [67].

• The "'loop-merging"'is another important program execution time enhancing mechanism [68]. Generally, it combines several actions of different independent loops into a single loop [69]. As a result, the execution time speeds up and we have applied this mechanism in our C version extensively.

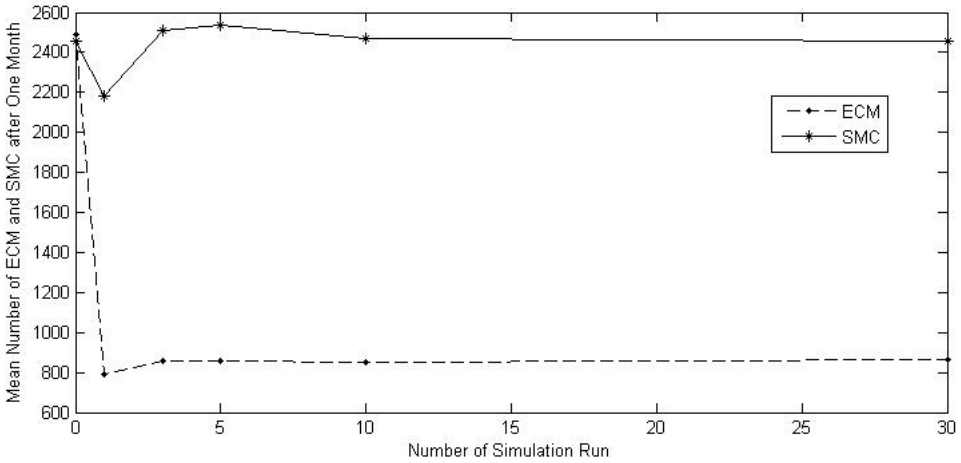

Figure 4.1: Convergence of SMC/ECM.

Apart from a fast execution time, the development is also modular to understand, debug and track of cellular activities in two dimensional spaces extensively. Additionally, two dimensional memory allocation is used to store information regarding cellular activities (i.e., cell type, internal clock time etc.). Since the cellular activities are associated with probabilities, monte-carlo simulation approach has been applied to find out the convergence of the number of cells/matrices. This requires the program to be run for different number of times and we observed an oscillatory relaxation pattern of number of cells/matrices - see Figure 4.1. This convergent result depends on the size of the system. A system of 121x121 sites takes about 15 runs to converge (Figure 4.1), while 241x241 takes about 10 runs to converge. The number of simulation results also depends on the number of parameters involved in the simulation program. As a result, we have incorporated parallel architecture into our implementation to facilitate fast execution and data collection of our simulation program, which we will follow up in the next section.

4.2 Parallel Architecture

Our ABM-PDE hybrid model has 15 parameters, where the first five has fixed value and the rest is sampled to test and validate with different hypothesis. As the range of values of the parameters increase, the number of test with different sets of values of the parameters also increases, which lead to the fact of introducing parallel implementation of our model. This parallel architecture of our model will definitely speed up in fast accumulation of the simulation results.

We have incorporated master-slave parallel architecture in our framework, where a single master processor is responsible to distribute parameter sets with different values and collect results from a number of slave processors. These slave processors are responsible to run the simulation for a specific period of time with a specific set of parameters. This master-slave parallel architecture ensures efficient utilization of the cluster machine, where it runs parallel simulations. If the number of required slave processors is greater than the number provided by the cluster machine, then the master processor assigns job to the specific number of slave processors provided by the cluster machine at first. As soon as a slave processor returns the simulation results back to the master processor, it assigns another job with another parameter sets to the slave processor and that is how the load balance is kept among the slave processors. Since the nonlinear sensitivity analysis requires sampling of the parameters in a large scale (i.e., $> 10^3$) [35], this parallel architecture certainly helps to get the results efficiently.

Each single processor has	Specification
CPU	1.6 GHz Intel Itanium 2 (128) processor
Memory	512 GB of global memory
Operating System	Red hat enterprise linux 5

Table 4.2: Specification of the cluster machine.

We have used 18 processors for the linear sensitivity analysis and 200 processors for the nonlinear sensitivity analysis simultaneously through the job submission system provided by the high performance computing center at the University of Houston.

To calculate the speed up factor of this master slave implementation, we can start with the equation Ts/Tp at first [70], where Ts is the execution time taken by a single processor to run the total number of simulations and Tp is the execution time taken by parallel processors to run the same number of simulation. Here $Tp = n/Tpn/ + cn/Tpn/ + Td$, where $n/Tpn/$ is the execution time taken by $n/$ number of processors for $n/$ number of simulations, Td is the data transfer time between master-slave processors and c is the number of times the slave processors have been assigned to perform simulation and $n = n/ + cn/$; where n is the total number of simulations. The more slave processors can be assigned jobs at first, the more speed up can be achieved for this kind of parallel implementation, since this will reduce the data distribution time (Td) among the master-slave processors for the rest of the simulation. .

4.3 Parallel GA-Model Implementation

We have coupled a genetic algorithm (GA) with the model to fit nonlinear histological data sets (sction 3.3). However, this data-fitting is an expensive operation which requires a lot of computing time. This requires an efficient implementation of the GA with the model to improve execution time. In this section, we would like to focus on this implementation details.

The GA has its own time convergence complexity [76] and the hybrid ABM-PDE model requires some computing time (Table 4.1). As a result, an efficient integration between the GA and the model is necessary to improve the overall execution time. The GA requires to have the fitness values of all of its populations to crossover and

mutate among the best populations [77]. The model receives the populations from the GA and calculates the fitness function and returns this to the GA. Since each population is independent of each other, the model can be executed with a number of populations simultaneously. As a result, we have incorporated our previous master-slave parallel architecture to couple the GA with the model (i.e., Figure 3.44).

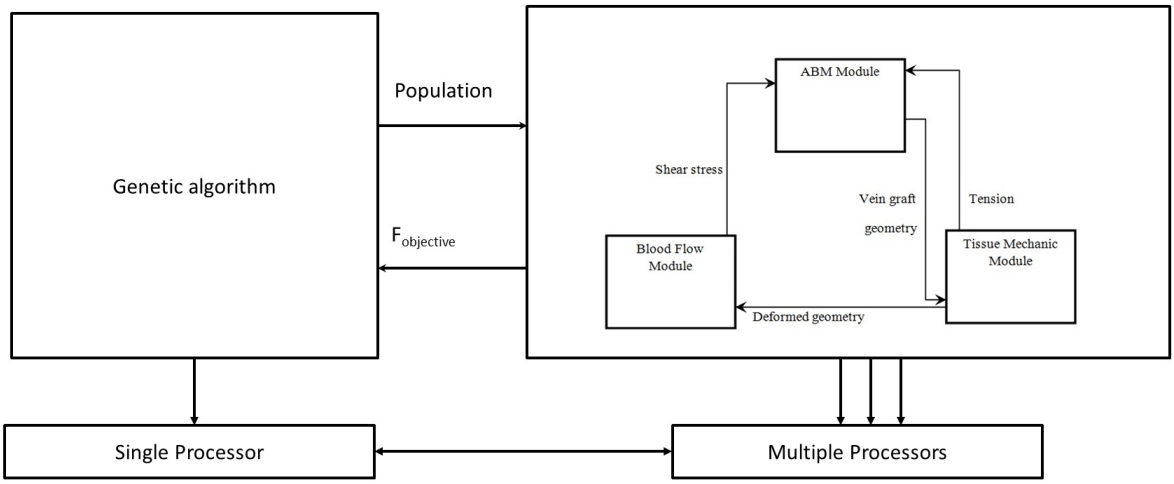

Figure 4.2: Master slave architecture of GA and the model.

One single processor (master) is responsible to run the GA, while a number of slave processors equal to the number of the populations will execute the model simultaneously (i.e., Figure 4.2). When a slave processor completes execution, it returns the value of the objective function (i.e., fitness value) to the master processor. The master processor waits for all the slave processors to receive the fitness value of the populations to move to the crossover and mutation step of the GA. So there is a delay in receiving the fitness value from all of the slave processors. This can be improved by applying asynchronous parallelism [78].

Chapter 5

Conclusion

Understanding the vascular adaptation is a difficult process, since there is a lot of uncertainty in predicting biological phenomena. Here we have introduced a bottom-up approach, where we can simulate cellular activities followed by the effect of mechanical environment as the shear stress and tension, which can answer some of the questions raised in the vascular adaptation ultimately. Our computational framework can generate patterns observed in the vascular adaptation and effective sets of parameters responsible for these patterns. This research finding can be extended to the gene regulatory system, which is responsible for the cellular activities and pattern formation. Once we can identify these genes, special drugs responsible for genetic activities can be introduced so that we can understand vascular adaptation from the genetic perspective.

We have applied the traditional translation of a medical discovery for the vascular adaptation here. This follows from the Petri dish to the animal model and finally, the

result is applied to the clinical application. Prior to this translation, a dual process to discovery is usually followed: observation from the clinical results and then the application of different hypotheses to verify the observation. But the difficulty arises from the incommensurability of the result of the animal model to the human model. As a result,we have introduced multiscale modeling (MSM) to solve this difficulty. The question we need to answer with the multiscale modeling covers a broad aspect. Can we refine the hypothesis for some specific experimental validation? When can a virtual experiment be considered a reasonable way to test a clinical hypothesis? How can we use models to optimize the experimental plan, design clinical trials accelerated translation, reduce the risk of therapeutic failure? How to go from MSM demonstration of mechanism to clinically-relevant measures (imaging, heat maps, physiologic variability, etc.) and back?

To address these questions, we are following the cycle: Hypothesis $->$ Model $->$ Simulation $->$ Experimental Validation, where we can update, test, refine our model every time we face any question to answer the stack holders (i.e., Surgeons, Mathematicians, Computer Scientists etc) of this project. According to this cycle, we build up main hypothesis regarding vascular adaptation in section 1. The hypothesis includes the probabilistic rules of cellular activities associated with the shear stress and tesnsion. These rules follow from the clinical and experimental results and observations.

Next, we incorporate the hypothesis into a computational framework to test different hypotheses in section 2. This framework has different modules to explain different scenarios in the vascular adaptation. As for example, we have the agent

based module to explain the cellular activities in a two dimensional space and the blood flow module and the tissue mechanic module to calculate shear stress and tension at the wall. As a result, our framework resembles the complex biological system of vascular adaptation, where the cellular activities are influenced by the external environmental conditions (i.e., shear stress and tension).

Our next goal is to test and validate the hypothesis associated with the clinical observation of the vascular adaptation with our computational framework and we have explained this in section 3. Generally, the vascular adaptation exhibits three types of patterns in clinical observations. We have generated these patterns virtually with the framework. We have analyzed the formation of each pattern individually and as a collection. As a result, these research findings can answer some of the fundamental questions associated with interesting pattern formations in the vascular adaptation.

These pattern matching schemes require a large number of computer simulations. These simulations take a lot of execution time. As a result, we have introduced single processor to multiple processor execution of the simulations to speed up execution and data collection from the results. Our implementation is scalable, modular and parallely efficient. We have applied different techniques used in high performance computing to improve our computing time, which we have discussed in section 4.

Therefore, we have given our best effort to define a computationally effective and efficient framework to understand vascular adaptation. Our goal is to prove that our framework is the best fit to explain vascular adaptation. Once we understand this adaptation from the cellular perspective thoroughly, we can introduce special drug

or gene-therapy to control this adaptation. As a result, this approach can be also applied in other similar interdisciplinary research fields to understand the underlying principal.

Chapter 6

Appendix

• **Analytical Solution for the Elasticity Model** : Here we will discuss the analytical solution of the tension and shear stress. The analytical modeling of the tension calculates the mechanical deformation at the cellular level. This analytical model calculates the radial stress σ_r, circumferential stress σ_θ and the displacement $u(r)$ of the number of cells which take part in SMC/ECM apoptosis/mitosis by the following equations:

$$\sigma_r(r) = p1r1^2(1 - r2^2/r^2)/(r2^2 - r1^2) - p2r2^2(1 - r1^2/r^2)/(r2^2 - r1^2), \quad (38)$$

$$\sigma_\theta(r) = p1r1^2(1 - r2^2/r^2)/(r2^2 + r1^2) - p2r2^2(1 - r1^2/r^2)/(r2^2 + r1^2), \quad (39)$$

$$u(r) = C_1/2r + C_2/r, \quad (40)$$

where $r1$ = radius of the lumen, $r2$ = radius of the EEL, $p1$ = The pressure on the lumen and $p2$ = The pressure on the EEL. The displacement is also associated with the following equation

$C_1 = (\lambda + \mu)(p1r1^2 - p2r2^2)/(r2^2 - r1^2)$ and (41)

$2\mu C_2 = (p1 - p2)r1^2r2^2/(r2^2 - r1^2)$, (42)

where λ and μ are the Lame coefficients: $\lambda = Ev/(1+v)(1-2v), \mu = E/2(1+v)$. Here E = Young modulus v = Poisson ratio. All of these calculations correspond to the boundary condition where E is 2000, v is 0.49 and $p1$ and $p2$ are 12.665625 N and 11.999013 N respectively.

• **Analytical Solution for Poiseuille Flow** : Now we will explain the analytical solution of shear stress. Blood flow exercises pressure and shear stress on the lumen wall. We assume a Poiseuille flow:

$Q = (\pi R^4_{lumen}\Delta P_{blood})/8\mu L$, (43)

where Q is the blood flow, P_{blood} is the pressure drop in a section of the vessel of length L, and μ is the dynamic viscosity. The shear stress at the wall is then given by the analytical formula:

$\tau = 2Umax/r1$, (44)

where $Umax = 0.3$ m/s is the maximum velocity of blood.

• **Calculation of** β : An ECM is surrounded by six SMCs at most. So β has the value between 1 and 6. We are interested about the particular value of β, which corresponds to the basic solution. So we run the simulation with different values of β (between 1 and 6) and then plot the ratio of ECM at the final hour to the initial hour.

We find the value of β corresponding to the basic solution (i.e., ecm ratio $\equiv$ 1 in

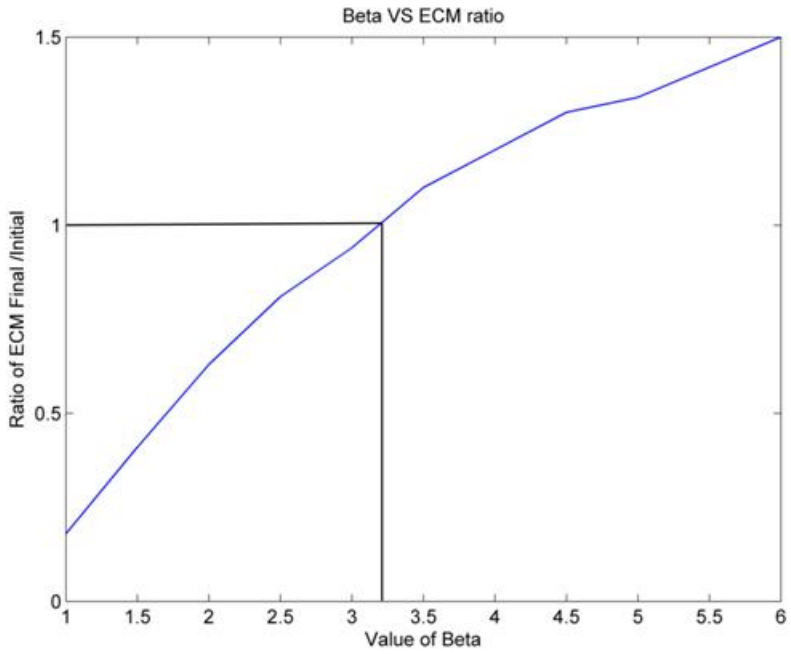

Figure 6.1: β VS ECM ratio.

figure 6.1) is 3.25. Next, we run the simulation while varying the value of β between (2 and 3.25) to find out the convergence of β. The simulation results show that β converges to 2.25, which has been used in the simulation of results of section 3.

Bibliography

[1] Marc Garbey, Mahbubur Rahman, and Scott A Berceli. A multi-scale computational framework to understand vascular adaptation. *Journal of Computational Science*, 2015.

[2] Marc Garbey and Scott A Berceli. A dynamical system that describes vein graft adaptation and failure. *Journal of Theoretical Biology*, 336:209–220, 2013.

[3] Minki Hwang, Marc Garbey, Scott A Berceli, Rongling Wu, Zhihua Jiang, and Roger Tran-Son-Tay. Rule-based model of vein graft remodeling. *PloS one*, 8(3):e57822, 2013.

[4] Anita C Thomas. Targeted treatments for restenosis and vein graft disease. *International Scholarly Research Notices*, 2012, 2012.

[5] Seymour Glagov. Intimal hyperplasia, vascular modeling, and the restenosis problem. *Circulation*, 89(6):2888–2891, 1994.

[6] Alexander M Bailey, Bryan C Thorne, and Shayn M Peirce. Multi-cell agent-based simulation of the microvasculature to study the dynamics of circulating inflammatory cell trafficking. *Annals of Biomedical Engineering*, 35(6):916–936, 2007.

[7] Ilana M Bayer, S Lee Adamson, and B Lowell Langille. Atrophic remodeling of the artery-cuffed artery. *Arteriosclerosis, thrombosis, and vascular biology*, 19(6):1499–1505, 1999.

[8] Francisco SA Cavalcante, Satoru Ito, Kelly Brewer, Hiroaki Sakai, Adriano M Alencar, Murilo P Almeida, José S Andrade Jr, Arnab Majumdar, Edward P Ingenito, and Béla Suki. Mechanical interactions between collagen and proteoglycans: implications for the stability of lung tissue. *Journal of Applied Physiology*, 98(2):672–679, 2005.

[9] Murray CH Clarke, Sara Talib, Nichola L Figg, and Martin R Bennett. Vascular smooth muscle cell apoptosis induces interleukin-1–directed inflammation effects of hyperlipidemia-mediated inhibition of phagocytosis. *Circulation Research*, 106(2):363–372, 2010.

[10] P Gerlee and Alexander RA Anderson. A hybrid cellular automaton model of clonal evolution in cancer: the emergence of the glycolytic phenotype. *Journal of Theoretical Biology*, 250(4):705–722, 2008.

[11] Franklin H Epstein, Gary H Gibbons, and Victor J Dzau. The emerging concept of vascular remodeling. *New England Journal of Medicine*, 330(20):1431–1438, 1994.

[12] E Javierre, FJ Vermolen, C Vuik, and S Van der Zwaag. A mathematical analysis of physiological and morphological aspects of wound closure. *Journal of Mathematical Biology*, 59(5):605–630, 2009.

[13] Manfred Lauth, Marc-Moritz Berger, Marco Cattaruzza, and Markus Hecker. Elevated perfusion pressure upregulates endothelin-1 and endothelin b receptor expression in the rabbit carotid artery. *Hypertension*, 35(2):648–654, 2000.

[14] Cornelis J Slager, Jolanda J Wentzel, Johan CH Schuurbiers, Jan AF Oomen, Jeroen Kloet, Rob Krams, Clemens Von Birgelen, Willem J Van Der Giessen, Patrick W Serruys, and Pim J De Feyter. True 3-dimensional reconstruction of coronary arteries in patients by fusion of angiography and ivus (angus) and its quantitative validation. *Circulation*, 102(5):511–516, 2000.

[15] Michael E DeBakey, Gerald M Lawrie, and Donald H Glaeser. Patterns of atherosclerosis and their surgical significance. *Annals of Surgery*, 201(2):115, 1985.

[16] Zhihua Jiang, Peng Yu, Ming Tao, Chessy Fernandez, Cristos Ifantides, Olajompo Moloye, Gregory S Schultz, C Keith Ozaki, and Scott A Berceli. Tgf-β-and ctgf-mediated fibroblast recruitment influences early outward vein graft remodeling. *American Journal of Physiology-Heart and Circulatory Physiology*, 293(1):H482–H488, 2007.

[17] Philip B Dobrin. Mechanical factors associated with the development of intimal and medial thickening in vein grafts subjected to arterial pressure a model of arteries exposed to hypertension. *Hypertension*, 26(1):38–43, 1995.

[18] Miguel Moyers-Gonzalez, Robert G Owens, and Jiannong Fang. A non-homogeneous constitutive model for human blood. part 1. model derivation and steady flow. *Journal of Fluid Mechanics*, 617:327–354, 2008.

[19] Scott A Berceli, Zhihua Jiang, Nina V Klingman, Chun L Pfahnl, Zaher S Abouhamze, Constanza D Frase, Gregory S Schultz, and C Keith Ozaki. Differential expression and activity of matrix metalloproteinases during flow-modulated vein graft remodeling. *Journal of Vascular Surgery*, 39(5):1084–1090, 2004.

[20] Zhihua Jiang, Scott A Berceli, Chun L Pfahnl, Lizhen Wu, Darin Goldman, Ming Tao, Motoko Kagayama, Akihiro Matsukawa, and C Keith Ozaki. Wall shear modulation of cytokines in early vein grafts. *Journal of Vascular Surgery*, 40(2):345–350, 2004.

[21] Chessy M Fernandez, Darin R Goldman, Zhihua Jiang, C Keith Ozaki, Roger Tran-Son-Tay, and Scott A Berceli. Impact of shear stress on early vein graft remodeling: a biomechanical analysis. *Annals of Biomedical Engineering*, 32(11):1484–1493, 2004.

[22] Scott A Berceli, Zhihua Jiang, Nina V Klingman, Gregory S Schultz, and C Keith Ozaki. Early differential mmp-2 and-9 dynamics during flow-induced arterial and vein graft adaptations. *Journal of Surgical Research*, 134(2):327–334, 2006.

[23] Zhihua Jiang, Lizhen Wu, Brett L Miller, Darin R Goldman, Chessy M Fernandez, Zaher S Abouhamze, C Keith Ozaki, and Scott A Berceli. A novel vein graft model: adaptation to differential flow environments. *American Journal of Physiology-Heart and Circulatory Physiology*, 286(1):H240–H245, 2004.

[24] Scott A Berceli, Mark G Davies, Richard D Kenagy, and Alexander W Clowes. Flow-induced neointimal regression in baboon polytetrafluoroethylene grafts is associated with decreased cell proliferation and increased apoptosis. *Journal of Vascular Surgery*, 36(6):1248–1255, 2002.

[25] Justin Sturge, S Katrina Todd, Giolanta Kogianni, Afshan McCarthy, and Clare M Isacke. Mannose receptor regulation of macrophage cell migration. *Journal of Leukocyte Biology*, 82(3):585–593, 2007.

[26] Oren Traub and Bradford C Berk. Laminar shear stress mechanisms by which endothelial cells transduce an atheroprotective force. *Arteriosclerosis, thrombosis, and vascular biology*, 18(5):677–685, 1998.

[27] Kenneth Walsh, Roy C Smith, and Hyo-Soo Kim. Vascular cell apoptosis in remodeling, restenosis, and plaque rupture. *Circulation Research*, 87(3):184–188, 2000.

[28] Stephen Wolfram. *Cellular automata and complexity: collected papers*, volume 1. Addison-Wesley Reading, 1994.

[29] Scott A Berceli, Roger Tran-Son-Tay, Marc Garbey, and Zhihua Jiang. Hemodynamically driven vein graft remodeling: a systems biology approach. *Vascular*, 17(suppl 1):S2–S9, 2009.

[30] M Garbey, BL Bass, and S Berceli. Multiscale mechanobiology modeling for surgery assessment. *Acta Mechanica Sinica*, 28(4):1186–1202, 2012.

[31] Minki Hwang, Marc Garbey, Scott A Berceli, and Roger Tran-Son-Tay. Rule-based simulation of multi-cellular biological systemsa review of modeling techniques. *Cellular and Molecular Bioengineering*, 2(3):285–294, 2009.

[32] Minki Hwang, Scott A Berceli, Marc Garbey, Nam Ho Kim, and Roger Tran-Son-Tay. The dynamics of vein graft remodeling induced by hemodynamic forces: a mathematical model. *Biomechanics and Modeling in Mechanobiology*, 11(3-4):411–423, 2012.

[33] Roger Tran-Son-Tay, Minki Hwang, Marc Garbey, Zhihua Jiang, C Keith Ozaki, and Scott A Berceli. An experiment-based model of vein graft remodeling induced by shear stress. *Annals of Biomedical Engineering*, 36(7):1083–1091, 2008.

[34] Jianxin Wang, Bo Chen, Yaqun Wang, Ningtao Wang, Marc Garbey, Roger Tran-Son-Tay, Scott A Berceli, and Rongling Wu. Reconstructing regulatory networks from the dynamic plasticity of gene expression by mutual information. *Nucleic acids research*, page gkt147, 2013.

[35] Simeone Marino, Ian B Hogue, Christian J Ray, and Denise E Kirschner. A methodology for performing global uncertainty and sensitivity analysis in systems biology. *Journal of Theoretical Biology*, 254(1):178–196, 2008.

[36] Marc Garbey, R Salmon, David Thanoon, and BL Bass. Multiscale modeling and distributed computing to predict cosmesis outcome after a lumpectomy. *Journal of Computational Physics*, 244:321–335, 2013.

[37] Christophe Geuzaine and Jean-François Remacle. Gmsh: A 3-d finite element mesh generator with built-in pre-and post-processing facilities. *International Journal for Numerical Methods in Engineering*, 79(11):1309–1331, 2009.

[38] William L Oberkampf, Timothy G Trucano, and Charles Hirsch. Verification, validation, and predictive capability in computational engineering and physics. *Applied Mechanics Reviews*, 57(5):345–384, 2004.

[39] Cendrine Mony, Marc Garbey, Malek Smaoui, and M-L Benot. Large scale parameter study of an individual-based model of clonal plant with volunteer computing. *Ecological Modelling*, 222(4):935–946, 2011.

[40] M Garbey and C Picard. A code-independent technique for computational verification of fluid mechanics and heat transfer problems. *Acta Mechanica Sinica*, 24(4):387–397, 2008.

[41] Christopher P Cheng, David Parker, and Charles A Taylor. Quantification of wall shear stress in large blood vessels using lagrangian interpolation functions with cine phase-contrast magnetic resonance imaging. *Annals of Biomedical Engineering*, 30(8):1020–1032, 2002.

[42] Hannan Tahir, Carles Bona-Casas, Andrew James Narracott, Javaid Iqbal, Julian Gunn, Patricia Lawford, and Alfons G Hoekstra. Endothelial repair process and its relevance to longitudinal neointimal tissue patterns: comparing histology with in silico modelling. *Journal of The Royal Society Interface*, 11(94):20140022, 2014.

[43] Colin J Boyle, Alex B Lennon, and Patrick J Prendergast. Application of a mechanobiological simulation technique to stents used clinically. *Journal of Biomechanics*, 46(5):918–924, 2013.

[44] Houman Zahedmanesh, Hans Van Oosterwyck, and Caitríona Lally. A multiscale mechanobiological model of in-stent restenosis: deciphering the role of matrix metalloproteinase and extracellular matrix changes. *Computer methods in Biomechanics and Biomedical Engineering*, 17(8):813–828, 2014.

[45] Haoyu Chen, Alisa Selimovic, Harry Thompson, Alessandro Chiarini, Justin Penrose, Yiannis Ventikos, and Paul N Watton. Investigating the influence of haemodynamic stimuli on intracranial aneurysm inception. *Annals of Biomedical Engineering*, 41(7):1492–1504, 2013.

[46] H Meng, VM Tutino, J Xiang, and A Siddiqui. High wss or low wss? complex interactions of hemodynamics with intracranial aneurysm initiation, growth, and rupture: toward a unifying hypothesis. *American Journal of Neuroradiology*, 2013.

[47] Marc Garbey, Barbara Lee Bass, Scott Berceli, Christophe Collet, and Pietro Cerveri. *Computational Surgery and Dual Training: Computing, Robotics and Imaging*. Springer, 2013.

[48] Andrea Saltelli, Stefano Tarantola, and KP-S Chan. A quantitative model-independent method for global sensitivity analysis of model output. *Technometrics*, 41(1):39–56, 1999.

[49] Gregory C Critchfield, Keith E Willard, and Donald P Connelly. Probabilistic sensitivity analysis methods for general decision models. *Computers and Biomedical Research*, 19(3):254–265, 1986.

[50] Cedric J Sallaberry, Jon C Helton, and Stephen C Hora. Extension of latin hypercube samples with correlated variables. *Reliability Engineering & System Safety*, 93(7):1047–1059, 2008.

[51] William J Conover and Ronald L Iman. Rank transformations as a bridge between parametric and nonparametric statistics. *The American Statistician*, 35(3):124–129, 1981.

[52] Francesca Campolongo and Andrea Saltelli. Sensitivity analysis of an environmental model: an application of different analysis methods. *Reliability Engineering & System Safety*, 57(1):49–69, 1997.

[53] Jon C Helton, Jay Dean Johnson, Cedric J Sallaberry, and Curt B Storlie. Survey of sampling-based methods for uncertainty and sensitivity analysis. *Reliability Engineering & System Safety*, 91(10):1175–1209, 2006.

[54] A Van Griensven, T Meixner, S Grunwald, T Bishop, M Diluzio, and R Srinivasan. A global sensitivity analysis tool for the parameters of multi-variable catchment models. *Journal of Hydrology*, 324(1):10–23, 2006.

[55] M Ratto, S Tarantola, and A Saltelli. Sensitivity analysis in model calibration: Gsa-glue approach. *Computer Physics Communications*, 136(3):212–224, 2001.

[56] Harvey M Wagner. Global sensitivity analysis. *Operations Research*, 43(6):948–969, 1995.

[57] Toshimitsu Homma and Andrea Saltelli. Importance measures in global sensitivity analysis of nonlinear models. *Reliability Engineering & System Safety*, 52(1):1–17, 1996.

[58] William J Welch, Robert J Buck, Jerome Sacks, Henry P Wynn, Toby J Mitchell, and Max D Morris. Screening, predicting, and computer experiments. *Technometrics*, 34(1):15–25, 1992.

[59] Mahbubur Rahman, Marc Garbey, and Scott A Berceli. Vein graft adaptation: Cross validation between a hybrid abm-pde model and a dynamical system. *Journal of Mechanobiology*, 2015 (To be submitted).

[60] Fujiichi Yoshimoto, Toshinobu Harada, and Yoshihide Yoshimoto. Data fitting with a spline using a real-coded genetic algorithm. *Computer-Aided Design*, 35(8):751–760, 2003.

[61] Carlos B Lucasius and Gerrit Kateman. Application of genetic algorithms in chemometrics. In *Proceedings of the third international conference on Genetic algorithms*, pages 170–176. Morgan Kaufmann Publishers Inc., 1989.

[62] Lawrence Davis. Adapting operator probabilities in genetic algorithms. In *International Conference on {G} enetic {A} lgorithms\'89*, pages 61–69, 1989.

[63] Jim Antonisse. A new interpretation of schema notation that overturns the binary encoding constraint. In *Proceedings of the third international conference on Genetic algorithms*, pages 86–91. Morgan Kaufmann Publishers Inc., 1989.

[64] Mahbubur Rahman and Marc Garbey. An efficient computational framework consists of a genetic algorithm and a hybrid abm-pde model to fit nonlinear histological data. *Journal of Parallel Computing*, 2015 (To be submitted).

[65] Paul R Wilson, Mark S Johnstone, Michael Neely, and David Boles. Dynamic storage allocation: A survey and critical review. In *Memory Management*, pages 1–116. Springer, 1995.

[66] Themistocles M Rassias and Peter Šemrl. On the mazur-ulam theorem and the aleksandrov problem for unit distance preserving mappings. *Proceedings of the American Mathematical Society*, 118(3):919–925, 1993.

[67] Vladmir Estivill-Castro and Derick Wood. A survey of adaptive sorting algorithms. *ACM Computing Surveys (CSUR)*, 24(4):441–476, 1992.

[68] Mark S Friedrichs, Peter Eastman, Vishal Vaidyanathan, Mike Houston, Scott Legrand, Adam L Beberg, Daniel L Ensign, Christopher M Bruns, and Vijay S Pande. Accelerating molecular dynamic simulation on graphics processing units. *Journal of Computational Chemistry*, 30(6):864–872, 2009.

[69] Ken Kennedy and Kathryn S McKinley. *Maximizing loop parallelism and improving data locality via loop fusion and distribution*. Springer, 1994.

[70] Hassan Chafi, Arvind K Sujeeth, Kevin J Brown, HyoukJoong Lee, Anand R Atreya, and Kunle Olukotun. A domain-specific approach to heterogeneous parallelism. In *ACM SIGPLAN Notices*, volume 46, pages 35–46. ACM, 2011.

[71] Vladimir Stojanovic and Vojin G Oklobdzija. Comparative analysis of master-slave latches and flip-flops for high-performance and low-power systems. *Solid-State Circuits, IEEE Journal of*, 34(4):536–548, 1999.

[72] Olivier Beaumont, Arnaud Legrand, and Yves Robert. The master-slave paradigm with heterogeneous processors. *Parallel and Distributed Systems, IEEE Transactions on*, 14(9):897–908, 2003.

[73] Marc Dubreuil, Christian Gagné, and Marc Parizeau. Analysis of a master-slave architecture for distributed evolutionary computations. *Systems, Man, and Cybernetics, Part B: Cybernetics, IEEE Transactions on*, 36(1):229–235, 2006.

[74] Guy Edjlali, Marc Garbey, and Damien Tromeur-Dervout. Interoperability parallel programs approach to simulate 3d frontal polymerization processes. *Parallel Computing*, 25(9):1161–1191, 1999.

[75] M Garbey and D Tromeur-Dervout. A parallel adaptive coupling algorithm for systems of differential equations. *Journal of Computational Physics*, 161(2):401–427, 2000.

[76] Carol A Ankenbrandt. An extension to the theory of convergence and a proof of the time complexity of genetic algorithms. In *FOGA*, pages 53–68, 1990.

[77] James Edward Baker. Adaptive selection methods for genetic algorithms. In *Proceedings of an International Conference on Genetic Algorithms and their applications*, pages 101–111. Hillsdale, New Jersey, 1985.

[78] Malek Smaoui Feki, Viet Huy Nguyen, and Marc Garbey. Parallel genetic algorithm implementation for boinc. In *PARCO*, pages 212–219, 2009.

[79] Tomasz Spalek, Piotr Pietrzyk, and Zbigniew Sojka. Application of the genetic algorithm joint with the powell method to nonlinear least-squares fitting of powder epr spectra. *Journal of Chemical Information and Modeling*, 45(1):18–29, 2005.

[80] Charles L Karr, Igor Yakushin, and Keith Nicolosi. Solving inverse initial-value, boundary-value problems via genetic algorithm. *Engineering Applications of Artificial Intelligence*, 13(6):625–633, 2000.

[81] Joshua B Tenenbaum, Vin De Silva, and John C Langford. A global geometric framework for nonlinear dimensionality reduction. *Science*, 290(5500):2319–2323, 2000.

[82] Alison L Marsden, Jeffrey A Feinstein, and Charles A Taylor. A computational framework for derivative-free optimization of cardiovascular geometries. *Computer methods in Applied Mechanics and Engineering*, 197(21):1890–1905, 2008.

[83] David Thanoon, Marc Garbey, Nam-Ho Kim, and Barbara Bass. A computational framework for breast surgery: application to breast conserving therapy. In *Computational Surgery and Dual Training*, pages 249–266. Springer, 2010.

[84] NK Schiller, T Franz, NS Weerasekara, P Zilla, and BD Reddy. A simple fluid–structure coupling algorithm for the study of the anastomotic mechanics of vascular grafts. *Computer methods in Biomechanics and Biomedical Engineering*, 13(6):773–781, 2010.